

SEARCH FOR SCALAR AND TENSOR UNPARTICLES IN THE DIPHOTON FINAL
STATE IN CMS EXPERIMENT AT THE LHC

A THESIS SUBMITTED TO
THE GRADUATE SCHOOL OF NATURAL AND APPLIED SCIENCES
OF
MIDDLE EAST TECHNICAL UNIVERSITY

BY

ILINA V. AKIN

IN PARTIAL FULFILLMENT OF THE REQUIREMENTS
FOR
THE DEGREE OF MASTER OF SCIENCE
IN
PHYSICS

SEPTEMBER 2009

Approval of the thesis:

**SEARCH FOR SCALAR AND TENSOR UNPARTICLES IN THE DIPHOTON FINAL
STATE IN CMS EXPERIMENT AT THE LHC**

submitted by **ILINA V. AKIN** in partial fulfillment of the requirements for the degree of
Master of Science in Physics Department, Middle East Technical University by,

Prof. Dr. Canan Özgen
Dean, Graduate School of **Natural and Applied Sciences**

Prof. Dr. Sinan Bilikmen
Head of Department, **Physics**

Prof. Dr. Mehmet T. Zeyrek
Supervisor, **Physics Department**

Examining Committee Members:

Prof. Dr. Ali Ulvi Yilmazer
Physics Department, Ankara University

Prof. Dr. Albert De Roeck
Physics Department, University of Antwerp/CERN

Prof. Dr. Mehmet T. Zeyrek
Physics Department, METU

Prof. Dr. Takhmasib M. Aliev
Physics Department, METU

Dr. Kazem Azizi
Physics Department, METU

Date:

I hereby declare that all information in this document has been obtained and presented in accordance with academic rules and ethical conduct. I also declare that, as required by these rules and conduct, I have fully cited and referenced all material and results that are not original to this work.

Name, Last Name: ILINA V. AKIN

Signature :

ABSTRACT

SEARCH FOR SCALAR AND TENSOR UNPARTICLES IN THE DIPHOTON FINAL STATE IN CMS EXPERIMENT AT THE LHC

Akin, Ilina Vasileva

M.S, Department of Physics

Supervisor : Prof. Dr. Mehmet T. Zeyrek

September 2009, 86 pages

We present a search for scalar and tensor unparticles in the diphoton final state produced in pp collisions at a center-of-mass energy of $\sqrt{s} = 10$ TeV, with the CMS detector at LHC. The analysis focuses on the data sample corresponding to the integrated luminosity of $\sim 100 \text{ pb}^{-1}$, expected to be collected in the first LHC run. The exclusion limits on unparticle parameters, scaling dimension d_U and coupling constant λ , and the discovery potential for unparticles are presented. This is the first simulation study of the sensitivity to unparticles decaying into the diphoton final state at a hadron collider.

Keywords: Unparticle, Diphotons, Large Extra Dimension, CMS, LHC

ÖZ

LHC'DEKİ CMS DENEYİNDE SKALAR VE TENSOR UNPARTICLE'LARIN ÇİFT FOTON SON DURUMDA ARAŞTIRILMASI

Akin, Ilina Vasileva

Yuksek Lisans, Fizik Bölümü

Tez Yöneticisi : Prof. Dr. Mehmet T. Zeyrek

Eylül 2009, 86 sayfa

Bu tezde 10 TeV kütle merkez enerjisindeki pp çarpışmalarında oluşan skalar ve tensor unparticle'ların çift foton final durumlarının LHC'deki CMS detektöründe incelendiği bir araştırmayı sunuyoruz. Analiz LHC'nin ilk çalışma zamanında toplanması öngörülen 100 pb^{-1} toplam ışınlığa denk gelen veri örneklemesine odaklanmıştır. Unparticle parametreleri üzerinde dışlama sınırları, d_U boyutu ile λ bağlaşım sabiti, ve bunların keşif potansiyelleri sunulmaktadır. Bu, bir hadron çarpıştırıcısının çift foton final durumuna bozulan unparticle'lara olan duyarlılığına dair ilk simülasyon çalışmasıdır.

Anahtar Kelimeler: Unparticle, Çift Foton, Geniş Ekstra Boyutlar, CMS, LHC

ACKNOWLEDGMENTS

This thesis could not have been written without the help of many people in many different ways.

Above all, I am most grateful to my adviser Prof. Mehmet Zeyrek for his continuous support, patience and kind insight. His enthusiasm and curiosity in high energy research are truly inspirational.

This thesis would not have been possible without the help and support of Albert de Roeck and Greg Landsberg. Their constant guidance and stimulating suggestions on different issues when doing the analysis on unparticles in diphoton final state were invaluable.

Especially, I would like to thank Prof. Meltem Serin who was the first to welcome me at METU and provide me with guidance over the last few years. Her encouragement and advices were extremely helpful for me to continue in this field.

I specially thank to Stefan Ask with whom we worked together on the validation of unparticle events generated with Pythia8. He was always very patient to explain everything in many details. Many thanks to Christophe Sout who helped me with the usage of Pythia8 Interface in CMSSW framework and gave solutions to different generation problems. I also thank Conor Henderson for the useful discussions about identification of photons in CMS.

I would like to thank Sezen Şekmen for her kindness and friendship, and all the time she spent helping me during my stay at CERN. Many thanks to Halil Gamsizkan, who was always too generous by helping me solving numerous problems with the CMSSW software. Also his assistance on Higgs analysis was invaluable.

I would like to thank all my lovely colleagues and friends for their friendship and support. In alphabetical order their names are Selçuk Bilmiş, Uğur Emrah Surat, Yasemin Uzunefe Yazgan and Efe Yazgan.

Especially, my deepest thanks to my husband Melih, who has been always beside me all these

years of hard work. Without him, the new road I have chosen to follow would have never been possible.

During the course of this work, I was supported by grants from TAEK.

TABLE OF CONTENTS

ABSTRACT	iv
ÖZ	v
ACKNOWLEDGMENTS	vi
TABLE OF CONTENTS	viii
LIST OF TABLES	xi
LIST OF FIGURES	xii
CHAPTERS	
1 INTRODUCTION	1
2 UNPARTICLES	4
2.1 Effective field theory	4
2.2 Unparticle theory	5
2.3 Phase space for scalar unparticle	7
2.4 Unparticle propagator	11
2.4.1 Scalar unparticle propagator	11
2.4.2 Vector and tensor unparticle propagator	12
2.5 Effective interactions	13
2.6 Direct production of unparticles	15
2.7 Virtual exchange of unparticles	17
2.8 Unparticle decay	18
2.9 Unparticle mass gap	20
2.10 Unparticle astrophysics and cosmology	21
2.10.1 Limits from astrophysics	22
2.10.2 Constraints from cosmology	22
2.11 Unparticle dark matter	23

3	THE LHC AND THE CMS EXPERIMENT	26
3.1	The LHC	26
3.2	CMS	29
3.2.1	Coordinate system	30
3.2.2	Superconducting magnet	30
3.2.3	Inner tracking system	30
3.2.4	Electromagnetic calorimeter	31
3.2.5	Hadron calorimeter	33
3.2.6	Muon system	34
3.2.7	The trigger system	35
3.2.8	Data acquisition system	36
3.2.9	CMS computing model	36
3.2.10	CMS offline software framework	38
3.3	Particle detection and measurement in CMS detector	38
4	SCALAR AND TENSOR UNPARTICLE PRODUCTION IN DIPHOTON FINAL STATE	43
4.1	The Photon	43
4.2	Event generation, detector simulation and reconstruction	44
4.2.1	Monte Carlo event generation	44
4.2.2	Detector simulation and reconstruction	46
4.3	Unparticle signal	48
4.3.1	Signal generation with Pythia8	48
4.3.2	Kinematical distributions	51
4.4	Background	56
4.4.1	SM diphoton production	57
4.4.1.1	LO processes	57
4.4.1.2	NLO processes	60
4.5	Analysis results with CMS software	62
4.6	Exclusion limits on unparticle production	63
4.6.1	Large extra dimensions and unparticles	63
4.6.2	95 % CL limit on cross section	65

4.6.3	Limits on unparticle parameters d_U and λ	65
4.7	Discovery potential for unparticle	69
4.7.1	Discovery potential for $500 < M_{\gamma\gamma} < 1000$ GeV invariant mass cut	69
4.7.2	Discovery potential for $600(700) < M_{\gamma\gamma} < 1000$ GeV invariant mass cut	71
4.8	Sensitivity to the unparticle model parameters without the perturbativity bound	74
5	CONCLUSIONS	77
	REFERENCES	79
APPENDICES		
A	KINEMATICAL VARIABLES IN HADRON COLLISIONS	81
B	SYSTEMATIC UNCERTAINTIES	84

LIST OF TABLES

TABLES

Table 2.1 Constraints on unparticles from energy loss from supernova SN 1987A, red giant and 5th force experiment [27].	22
Table 3.1 Design parameters of the LHC.	28
Table 3.2 Particle detection in different CMS layers.	42
Table 4.1 LO scalar and tensor unparticle cross sections for $\Lambda_{\mathcal{U}} = 1$ TeV as a function of the scale dimension parameter and the coupling constant.	51
Table 4.2 95% CL limit on the signal cross section ($\mathcal{U} \rightarrow \gamma\gamma$) for a signal in the diphoton channel for $500 \text{ GeV} < M_{\gamma\gamma} < 1000 \text{ GeV}$ and the expected number of background events in the same region [45].	66
Table 4.3 LO scalar and tensor unparticle cross sections in the control $200 \text{ GeV} < M_{\gamma\gamma} < 500 \text{ GeV}$ (ΔS_c) and signal $500 \text{ GeV} < M_{\gamma\gamma} < 1000 \text{ GeV}$ (ΔS_s) regions, along with the correction factors f and rescaled cross section in the signal region ($\Delta S'_s$) used for limit setting and discovery potential estimate.	67
Table 4.4 f_B factor for scalar and tensor unparticles.	70
Table 4.5 Luminosity needed for observation or discovery given spin-0 and spin-2 unparticle parameters for $500 \text{ GeV} < M_{\gamma\gamma} < 1000 \text{ GeV}$	71
Table 4.6 LO scalar and tensor unparticle cross sections in the control $200 \text{ GeV} < M_{\gamma\gamma} < 500 \text{ GeV}$ (ΔS_c) and signal $M_{\gamma\gamma} > 500 \text{ GeV}$ (ΔS_s) regions, along with the correction factors f and rescaled cross section in the signal region ($\Delta S'_s$) used for limit setting and discovery potential estimate.	74
Table 4.7 Luminosity needed for observation or discovery given spin-0 and spin-2 unparticle parameters for $M_{\gamma\gamma} > 500 \text{ GeV}$	76

LIST OF FIGURES

FIGURES

Figure 2.1 Comparison of the prediction for the monojet E_T distribution in the ADD model with $M_D = 4$ TeV and $\delta = 2$ (red) with scalar (green and magenta) and vector (blue) unparticle for chosen unparticle parameters. SM background is shown in black [16].	16
Figure 2.2 Number of events with $10fb^{-1}$ as a function of the mass gap μ . The solid (red) line corresponds to prompt events, the dot-dashed (blue) line corresponds to monojet events and the dashed (green) line corresponds to delayed events [20]. . .	20
Figure 2.3 The relic abundance of the unparticle dark matter as a function of the Higgs boson mass for given unparticle masses, together with constraint on the relic abundance from WMAP measurement [30].	24
Figure 2.4 The relic abundance of the unparticle dark matter. The shaded area is the allowed region for the WMAP measurements at 2σ confidence level [30].	24
Figure 3.1 The layout of the Large Hadron Collider.	27
Figure 3.2 A perspective view of the CMS detector [32].	29
Figure 3.3 Layout of the CMS ECAL showing the arrangement of crystal modules, supermodules and endcaps [32].	32
Figure 3.4 CMS HCAL barrel in hadron calorimeter [32].	34
Figure 3.5 Muon chambers at CMS detector [32].	35
Figure 3.6 Architecture of the L1 trigger [32].	36
Figure 3.7 Modules within the CMS Framework [32].	39
Figure 4.1 Pythia processes.	46

Figure 4.2 Single Pythia event listing and integrated cross sections for spin-0 unparticle with $\lambda_s = 0.9$, $d_{\mathcal{U}} = 1.01$ and $\Lambda_{\mathcal{U}} = 1$ TeV in diphoton final state.	52
Figure 4.3 Invariant mass distribution for spin-0 (left) and spin-2 (right) unparticle, plotted for various values of dimension parameter $d_{\mathcal{U}}$ with $\Lambda_{\mathcal{U}} = 1$ TeV and λ_s , $\lambda_t = 0.9$	53
Figure 4.4 Invariant mass distribution for spin-0 (left) and spin-2 (right) unparticle with $\Lambda_{\mathcal{U}} = 1$ TeV and $d_{\mathcal{U}} = 1.01$, plotted for various values of the couplings λ_s and λ_t	54
Figure 4.5 Angular distribution for spin-0 (left) and spin-2 (right) unparticle with $\Lambda_{\mathcal{U}} = 1$ TeV and $d_{\mathcal{U}} = 1.01$, plotted for various values of the couplings λ_s and λ_t	55
Figure 4.6 Rapidity distribution of diphoton system for spin-0 (left) and spin-2 (right) unparticle with $\Lambda_{\mathcal{U}} = 1$ TeV and $d_{\mathcal{U}} = 1.01$, plotted for various values of the couplings λ_s and λ_t	55
Figure 4.7 Feynman diagrams for the Born subprocess $q\bar{q} \rightarrow \gamma\gamma$. The straight and wavy lines denote quarks and photons, respectively [46].	57
Figure 4.8 Feynman diagrams for the Box subprocess $gg \rightarrow \gamma\gamma$. The straight, wavy and curly lines denote quarks, photons and gluons, respectively [46].	60
Figure 4.9 Feynman diagrams for the virtual subprocess $q\bar{q} \rightarrow \gamma\gamma$ [46].	61
Figure 4.10 Feynman diagrams for the real emission process $q\bar{q} \rightarrow \gamma\gamma g$ [46].	62
Figure 4.11 Diphoton invariant mass distribution for different backgrounds as well as scalar (left) and tensor (right) unparticle production. Lower limit on diphoton invariant mass of 500 GeV shown with a vertical red line, set to find limits on unparticle parameters and discovery potential.	64
Figure 4.12 Spin-0 unparticle cross section parametrization as a function of $d_{\mathcal{U}}$ for $\lambda_s = 0.9$ (left) and λ_s for $d_{\mathcal{U}} = 1.01$ (right) for $500 < M_{\gamma\gamma} < 1000$ GeV.	68
Figure 4.13 Spin-2 unparticle cross section parametrization as a function of $d_{\mathcal{U}}$ for $\lambda_t = 0.9$ (left) and λ_t for $d_{\mathcal{U}} = 1.01$ (right) for $500 < M_{\gamma\gamma} < 1000$ GeV.	69

Figure 4.14 Luminosity required for for spin-0 and spin-2 unparticle discovery for $500 \text{ GeV} < M_{\gamma\gamma} < 1000 \text{ GeV}$. Different lines correspond to different model parameters. Subsequent points on the lines correspond to sequential integer number of expected events; points corresponding to 1, 3, and 5 events are marked correspondingly.	72
Figure 4.15 Luminosity required for for spin-0 and spin-2 unparticle discovery for $600 \text{ GeV} < M_{\gamma\gamma} < 1000 \text{ GeV}$. Different lines correspond to different model parameters. Subsequent points on the lines correspond to sequential integer number of expected events; points corresponding to 1, 3, and 5 events are marked correspondingly.	73
Figure 4.16 Luminosity required for for spin-0 and spin-2 unparticle discovery for $700 \text{ GeV} < M_{\gamma\gamma} < 1000 \text{ GeV}$. Different lines correspond to different model parameters. Subsequent points on the lines correspond to sequential integer number of expected events; points corresponding to 1, 3, and 5 events are marked correspondingly.	73
Figure 4.17 Spin-0 unparticle cross section parametrization as a function of $d_{\mathcal{U}}$ for $\lambda_s = 0.9$ (left) and λ_s for $d_{\mathcal{U}} = 1.01$ (right) for $M_{\gamma\gamma} > 500 \text{ GeV}$	75
Figure 4.18 Spin-2 unparticle cross section parametrization as a function of $d_{\mathcal{U}}$ for $\lambda_t = 0.9$ (left) and λ_t for $d_{\mathcal{U}} = 1.01$ (right) for $M_{\gamma\gamma} > 500 \text{ GeV}$	75
Figure 4.19 Luminosity required for for spin-0 and spin-2 unparticle discovery for $M_{\gamma\gamma} > 500 \text{ GeV}$. Different lines correspond to different model parameters. Subsequent points on the lines correspond to sequential integer number of expected events; points corresponding to 1, 3, and 5 events are marked correspondingly. . .	76

CHAPTER 1

INTRODUCTION

It is widely believed that the Standard Model (SM) [1], [2], [3] is not a complete theory of particle physics, and that there is a new physics sector coupled to the SM, which can solve various problems of the SM such as the hierarchy problem, baryon asymmetry of the universe and the identity of dark matter. This new physics can have several forms. It can be weakly coupled like supersymmetric theories or strongly coupled like technicolor. Supersymmetric theories for example solve many problems in contemporary particle physics including hierarchy problem. It has also additional sources of CP violation and dark matter candidates but introduce too many particles which have still not been seen. Apart from verifying the SM expectations there is also another option - existence of a completely new physics scale invariant sector. This is the idea of unparticles that was introduced by H.Georgi. He suggests that there is a sector that is exactly scale invariant and very weakly interacting with the SM sector. The tool that is used to describe this new sector of unparticle physics is effective field theory [4] which is valid below a cut off scale Λ_U . The main idea is that while the detailed physics with a nontrivial scale invariant infrared fixed point is nonlinear and complicated at high energy scale (M_U), the low energy effective field theory for $\Lambda_U < M_U$ can be very simple because of scale invariance. The most relevant theories close to unparticle concept are the theories of extra dimensions (Randall - Sundrum model) and unparticles are considered to be a simplified version of these models.

In classical physics, the energy, linear momentum and mass of a free point particle are linked through the relativistic equation [5]

$$E^2 = p^2 + m^2 \tag{1.1}$$

where the speed of light is taken to be $c = 1$. Quantum mechanics converts Eq. 1.1 into a dispersion relation for the corresponding quantum waves, with wave number k , mass m and low frequency cut-off ω (the Plank's constant is taken to be $\hbar = 1$ and the speed of light $c = 1$)

$$\omega^2 = k^2 + m^2. \quad (1.2)$$

Unlike Equations 1.1 and 1.2, unparticles emerge as fractional objects which have non-integral scaling dimensions, something that has never been seen before. The scale-invariant world of unparticles is hidden from us at low energies because its interactions with the SM particles are so weak. However if they interact, these particle interactions would appear to have missing energy and momentum distributions. In that meaning, unparticles resemble very much neutrinos. For example, neutrinos are nearly massless and therefore nearly scale invariant. They couple very weakly to the ordinary matter at low energies, and the effect of the coupling increases as the energy increases. It has been suggested that the existence of unparticles enables a natural explanation for breaking of space-time symmetries in weak interactions. They can give a solution to some of the problems existing in the SM like being a new source for flavor and CP violation and dark matter candidate.

The structure of the thesis is as follows:

In Chapter 2 we give a short introduction to unparticle theory, show some examples of unparticle interaction with SM fields and their possible signatures in colliders. At the end, we quote some of the astrophysical constraints that are imposed on unparticle parameters and discuss the existence of unparticle as possible dark matter candidate.

In Chapter 3 is described the CMS detector at LHC, that is used for the simulation and detection of unparticles decaying to a pair of photons. In the focus of our view is the ECAL subdetector where the detection and identification of photons mainly occurs. At the end of this chapter we explain how particles are generally detected in the different subdetectors and discuss methods for their identification.

Chapter 4 describes the search for scalar and tensor unparticle in diphoton final state with CMS detector at LHC. Our study is mainly focused on scalar unparticles but for completeness of this work we give results for tensor unparticles as well. We show unparticle's invariant mass distribution for different unparticle set of parameters for spin-0 and spin-2 unparticle as

an enhancement over the SM Born background which is the main background to our signal. Using Bayesian approach, exclusion limits on the unparticle parameters, scaling dimension $d_{\mathcal{U}}$ and coupling constant λ are set. We quote the luminosities needed to observe spin-0 and spin-2 unparticles within the first LHC runs by taking into account the exclusion limits set on the unparticle parameters.

Chapter 5 is a summary of the results obtained in Chapter 4.

CHAPTER 2

UNPARTICLES

2.1 Effective field theory [4]

We live in a world in which there seems to exist interesting physics at all scales. To do physics easier, it is convenient to be able to isolate a set of phenomena from all the rest and to describe it without having to understand everything. In that meaning the parameter space of the world is divided into different regions, in each of which there is different description of physics. Therefore effective field theory is an approximate theory that describes physical phenomena occurring at a chosen length scale while ignoring phenomena at shorter distances or higher energies. Effective field theory describes physics at a given energy scale E , to a given accuracy ϵ , in terms of quantum field theory with a finite set of parameters. The effect of physics at higher energies on the physics at the scale E is described by series of interactions with integral mass dimension from two to infinity for renormalizable interactions and including nonrenormalizable interactions of arbitrary high dimensions. The principles of the effective field theory are:

1. There are finite number of parameters that describe the interactions of each dimension, $k - 4$;
2. The coefficients of each of the interaction terms of dimension $k - 4$ is less than or of order of

$$\frac{1}{M^k} \quad \text{where } E < M \quad (2.1)$$

for mass M that is independent from dimension k .

These conditions ensure that only a finite number of parameters are required to calculate physical quantities at energy E to an accuracy ϵ , because the contribution of interactions is proportional to

$$\left(\frac{E}{M}\right)^k. \quad (2.2)$$

Thus the terms that are included in the calculations are up to dimension k_ϵ of which there are only finite numbers

$$\left(\frac{E}{M}\right)^{k_\epsilon} \approx \epsilon \quad \Rightarrow \quad k_\epsilon \approx \frac{\ln(1/\epsilon)}{\ln(M/E)}. \quad (2.3)$$

Going up in the energy scale, the nonrenormalizable interactions for any fixed k becomes more important. k_ϵ increases and before energies of order M , the nonrenormalizable interactions disappear and become renormalizable. Then there is a new effective theory and the process starts over again.

If we could have one theory valid at all scales it would not be necessary to use effective theories. However due to our ignorance at high energy scales we put some constraints and try to describe physics only in a given region.

2.2 Unparticle theory [6]

Unparticle theory is an example of low energy effective theory valid below some scale Λ_U . This theory introduces a new idea [7] of a scale invariant sector in the SM that interacts very weakly with those sectors of the SM that have already been observed. The objects that make that sector, have been given the name unparticles. In order to study the new sector one can use ideas from Conformal Field Theories (CFT). Conformal (scale invariant) theory is a quantum field theory that is invariant under conformal transformations. The necessary conditions for a quantum field theory to be scale invariant are:

- There are no dimensional parameters like masses;
- At quantum level there is a need of a fixed point of all β functions.

Scale invariance has been known since many years in the physics world. Near a fixed point (critical point), field theories show scale invariance. A theory is said to have fixed point once the β function for the theory vanishes. The β function is Callan - Symanzik function which reflects the change in the coupling constant of the theory as the mass scale increases. In general, β vanishes when going to smaller mass scales at zero coupling constant.

It was mentioned before that unparticle theory is a low energy effective theory. To get there, in Quantum Field Theory (QFT) there is a standard procedure that uses a renormalization group flows. This means that one can change the mass scale of the theory by a multiplicative factor. Such process rescales every field that has a non-zero mass dimension by the same factor raised to the power of the mass dimension of the field. Mass rescaling can not change the zero mass of an object, therefore the theory of a free massless particle is scale invariant.

First the idea of a theory with scale invariance in the infrared was put forward by Banks-Zaks (\mathcal{BZ}) [8] who studied gauge theories with non-integral number of fermions. These theories have conformal invariance which implies scale invariance or theory looks the same at all scales. The SM is not conformal theory since couplings depend on scale and the Higgs mass breaks the conformal invariance. According to [7] at very high energies ($E > \Lambda_U$) theory contains both fields of the SM and fields of \mathcal{BZ} sector with non-trivial infra-red (\mathcal{IR}) fixed point. An infra-red fixed point corresponds to a non-trivial value of the coupling constant. The SM sector and the hidden \mathcal{BZ} sector interact via the exchange of particles of very large mass M_U and they are coupled through non-renormalizable couplings. The interaction below some scale M_U takes the form

$$\frac{O_{SM}O_{\mathcal{BZ}}}{M_U^k} \quad (2.4)$$

where O_{SM} is SM operator of mass dimension d_{SM} , $O_{\mathcal{BZ}}$ is ultra-violet \mathcal{BZ} operator of mass dimension $d_{\mathcal{BZ}}$ and the total mass dimension of the new term is

$$d = d_{SM} + d_{\mathcal{BZ}} - k. \quad (2.5)$$

In four spacetime dimensions $d = 4$, in order for the action to be dimensionless

$$k = d_{SM} + d_{\mathcal{BZ}} - 4. \quad (2.6)$$

Moving down the energy scale from $M_{\mathcal{U}}$ to $\Lambda_{\mathcal{U}}$ the hidden sector becomes conformal and the \mathcal{BZ} operators $O_{\mathcal{BZ}}$ above scale $\Lambda_{\mathcal{U}}$ flow to the unparticle operator $O_{\mathcal{U}}$ for $E < \Lambda_{\mathcal{U}}$. $\Lambda_{\mathcal{U}}$ is the scale at which dimensional transmutation occurs. If unparticle operator $O_{\mathcal{U}}$ has mass dimension $d_{\mathcal{U}}$ then

$$O_{\mathcal{BZ}} = C_{\mathcal{U}} \Lambda_{\mathcal{U}}^{d_{\mathcal{BZ}} - d_{\mathcal{U}}} O_{\mathcal{U}} \quad (2.7)$$

where $C_{\mathcal{U}}$ is a coefficient in the low energy effective theory expected to be of order 1.

Using Equation 2.7 one can rewrite 2.4 to obtain the coupling of the unparticle operator $O_{\mathcal{U}}$ with the SM operator O_{SM} in the low energy effective theory

$$\frac{C_{\mathcal{U}} \Lambda_{\mathcal{U}}^{d_{\mathcal{BZ}} - d_{\mathcal{U}}}}{M_{\mathcal{U}}^k} O_{SM} O_{\mathcal{U}} = \lambda O_{SM} O_{\mathcal{U}} \quad (2.8)$$

where λ is the new coupling constant which has mass dimension $d_{\lambda} = d_{\mathcal{BZ}} - d_{\mathcal{U}} - k$. $M_{\mathcal{U}}$ must be much larger than the scale $\Lambda_{\mathcal{U}}$ so that the coupling constant λ is very small for unparticle fields to not couple strongly enough to ordinary matter to have been detected.

We do not know anything about scale invariant sector above TeV scale but using the effective field theory below the scale $\Lambda_{\mathcal{U}}$ one should be able to see unparticles at LHC.

2.3 Phase space for scalar unparticle [9]

It was shown in Chapter 1 that all dimensional quantities, time and space, are tied together and therefore must scale together. If time and space are scaled up, energy and momentum must be scale down. In classical physics and quantum mechanics there is a fixed non-zero mass m that breaks the scale-invariance. Energy and momentum can not be scaled without changing the mass m . Therefore only theories of free massless relativistic particles have scale invariance.

If a state of free massless particles exists with (E_j, \vec{p}_j) , one can always make a scaled state with $(\lambda E_j, \lambda \vec{p}_j)$. Fermi's Golden Rule is a way to calculate the transition rate which is probability of transition per unit time from one energy eigenstate of a quantum system into a continuum of energy eigenstates and is given by the equation

$$P_{if} = \frac{2\pi}{\hbar} |M_{if}|^2 \rho_f \quad (2.9)$$

where $|M_{if}|$ is the amplitude of the process and ρ_f is the density of final states. ρ_f can be expressed also as a number of quantum states in a cubical box with side l . Due to the periodic boundary conditions in the box

$$\vec{p} = 2\pi\vec{n}/l. \quad (2.10)$$

The phase space of the free massless particles is given by

$$d\rho(p) = \frac{\text{\#states}}{l^3} = \frac{d^3 p}{(2\pi)^3} \quad (2.11)$$

and its relativistic form is

$$d\rho(p) = \frac{d^3 p}{2E(2\pi)^3} = \theta(p^0)\delta(p^2)\frac{d^4 p}{(2\pi)^3}. \quad (2.12)$$

If there is one massless particle, its phase space $d\rho_1$ is defined as

$$d\rho_1(p) = \frac{d^3 p}{2E(2\pi)^3} = \theta(p^0)\delta(p^2)\frac{d^4 p}{(2\pi)^3} \quad (2.13)$$

with $E = p^0 = |\vec{p}|$.

If there are two massless particles in the final state that we do not see and all we know is their total energy-momentum P , the combination of their phase spaces is given by

$$\begin{aligned} & \left(\int \delta^4 \left(P - \sum_{j=1}^2 p_j \right) \prod_{j=1}^2 \delta(p_j^2) \theta(p_j^0) \frac{d^4 p_j}{(2\pi)^3} \right) d^4 P \\ & \equiv d\rho_2(P) = \frac{1}{8\pi} \theta(P^0) \theta(P^2) \frac{d^4 P}{(2\pi)^4}. \end{aligned} \quad (2.14)$$

For n massless particles the spectral density function is

$$\begin{aligned} d\rho_n(P) &= \left(\int \delta^4 \left(P - \sum_{j=1}^2 p_j \right) \prod_{j=1}^2 \delta(p_j^2) \theta(p_j^0) \frac{d^4 p_j}{(2\pi)^3} \right) d^4 P \\ &= A_n \theta(P^0) \theta(P^2) \theta(P^2)^{n-2} \frac{d^4 P}{(2\pi)^4} \end{aligned} \quad (2.15)$$

with

$$A_n = \frac{16\pi^{5/2}}{(2\pi)^{2n}} \frac{\Gamma(n+1/2)}{\Gamma(n-1)\Gamma(2n)}. \quad (2.16)$$

Now lets look at the two point function of a scalar unparticle operator $O_{\mathcal{U}}$. It has the following form

$$\begin{aligned} \langle 0 | O_{\mathcal{U}}(x) O_{\mathcal{U}}^\dagger(0) | 0 \rangle &= \langle 0 | e^{i\hat{P}\cdot x} O_{\mathcal{U}}(0) e^{-i\hat{P}\cdot x} O_{\mathcal{U}}^\dagger(0) | 0 \rangle \\ &= \int d\lambda \int d\lambda' \langle 0 | O_{\mathcal{U}}(0) | \lambda' \rangle \langle \lambda' | e^{-i\hat{P}\cdot x} | \lambda \rangle \langle \lambda | O_{\mathcal{U}}^\dagger(0) | 0 \rangle \\ &= \int \frac{d^4 P}{(2\pi)^4} e^{-i\hat{P}\cdot x} \rho_{\mathcal{U}}(P^2) \end{aligned} \quad (2.17)$$

where $\rho_{\mathcal{U}}(P^2)$ is the spectral density given by

$$\rho_{\mathcal{U}}(P^2) = (2\pi)^4 \int d\lambda \delta^4(P - p_\lambda) |\langle 0 | O_{\mathcal{U}}(0) | \lambda \rangle|^2. \quad (2.18)$$

Since Equation 2.18 is a scalar function it can depend on (P^2) and $\theta(P^0)$ and therefore

$$\rho_{\mathcal{U}}(P^2) = A_{d_{\mathcal{U}}} \theta(P^0) \theta(P^2) (P^2)^\alpha \quad (2.19)$$

where $A_{d_{\mathcal{U}}}$ and α are dimensionless constants that depend on the scale invariant theory. The scale invariance implies that $\alpha = d_{\mathcal{U}} - 2$ [10]. It is easily seen, after comparison with Equation 2.15, that Equation 2.19 corresponds to phase space of n massless particles of total momentum P with phase space $A_n \theta(P^0) \theta(P^2) (P^2)^{n-2}$.

It follows that unparticles look the same as $d_{\mathcal{U}}$ massless particles, where $d_{\mathcal{U}} \rightarrow n$ and $A_{d_{\mathcal{U}}} \rightarrow A_n$ with

$$A_{d_{\mathcal{U}}} = \frac{16\pi^{5/2}}{(2\pi)^{2d_{\mathcal{U}}}} \frac{\Gamma(d_{\mathcal{U}} + \frac{1}{2})}{\Gamma(d_{\mathcal{U}} - 1)\Gamma(2d_{\mathcal{U}})}. \quad (2.20)$$

The conclusion is that for fractional $d_{\mathcal{U}}$, the objects created by $O_{\mathcal{U}}$ can not be ordinary particles but instead something else which is named as unparticles.

If we allow an interaction between unparticles and standard model particles, this takes the following form

$$\epsilon O_{SM} O_{\mathcal{U}} \quad \text{where} \quad \epsilon = \frac{\Lambda_{\mathcal{U}}^{d_{\mathcal{B}Z} - d_{\mathcal{U}}}}{M_{\mathcal{U}}^k}. \quad (2.21)$$

After inserting some standard model process $SM_{in/out}$ in Equation 2.21

$$\epsilon^2 |\langle SM_{out} | O_{SM} | SM_{in} \rangle \langle \mathcal{U} | O_{\mathcal{U}} | 0 \rangle|^2 \quad (2.22)$$

the result is a production of unparticle which is equivalent to missing energy and momentum. The probability distribution of the above interaction is proportional to the phase space for scale invariant unparticle which goes like $d\rho_{\mathcal{U}}$ and looks like the production of $d_{\mathcal{U}}$ massless particles. All this can be shown in more details by working out the unparticle propagator. It will be discussed in the following chapter.

In conclusion, unparticles are:

- **The particle formulation:**

All particles are either massless or their mass spectra are continuous. In the SM theory there are plenty of particles with non-zero masses however in a scale invariant theory we can not have a definite mass unless it is zero.

- **The field formulation:**

Scale invariant fields have no particle excitations with definite mass other than zero. The "response" of the field to an injection of energy is not particle creation, but an effective dissipation of energy. This field is called unparticle.

2.4 Unparticle propagator [10]

2.4.1 Scalar unparticle propagator

Scale invariance almost determines unparticle propagator completely. In momentum space the propagator for scalar unparticle can be written as a dispersion integral

$$\begin{aligned}\Delta_F(P^2) &= \frac{1}{2\pi} \int_0^\infty \frac{A_{du}(M^2)^{d_u-2} dM^2}{P^2 - M^2 + i\epsilon} \\ &= \frac{1}{2\pi} \int_0^\infty \frac{A_{du}(M^2)^{d_u-2} dM^2}{P^2 - M^2} - i\frac{1}{2} A_{du}(P^2)^{d_u-2} \theta(P^2)\end{aligned}\quad (2.23)$$

with A_{du} defined in Equation 3.5.

In order $\Delta_F(P^2)$ to be scale invariant it is assumed that $\Delta_F(P^2) = Z_{du}(-P^2)^{d_u-2}$ [10], where Z_{du} is a factor to be determined. The complex function $(-P^2)^{d_u-2}$ has the following values

$$(-P^2)^{d_u-2} = \begin{cases} |P^2|^{d_u-2} & P^2 < 0 \quad \text{No complex phase} \\ |P^2|^{d_u-2} \exp(-id_{u\pi}) & P^2 > 0 \quad \text{Complex phase} \end{cases}\quad (2.24)$$

For time-like momenta, when $P^2 > 0$

$$Z_{du} = \frac{A_{du}}{2 \sin(d_{u\pi})}\quad (2.25)$$

and the final form for scalar unparticle propagator is

$$\Delta_F(P^2) = \frac{A_{du}}{2 \sin(d_{u\pi})} (-P^2)^{d_u-2}.\quad (2.26)$$

This shows that the propagator can be understood as a sum over resonances with their masses continuously distributed.

When $d_{\mathcal{U}} \rightarrow 1 + \epsilon$, for small positive ϵ , the standard results can be obtained

$$\lim_{d_{\mathcal{U}} \rightarrow 1 + \epsilon} \Delta_F(P^2) = \frac{1}{P^2}. \quad (2.27)$$

The constraints on scalar unparticle dimensions $d_{\mathcal{U}}$ are [11]:

- Lower bound: $d_{\mathcal{U}} > 1$ imposed by unitarity.
- Upper bound: $d_{\mathcal{U}} < 2$ because for $d_{\mathcal{U}} > 2$ the propagator becomes infinite.

In general, for large values of $d_{\mathcal{U}}$ the interaction between unparticles and SM particles becomes too weak.

2.4.2 Vector and tensor unparticle propagator

In a similar way as it was done for scalar unparticle, the two point function and propagator can be derived for vector and tensor unparticle. The vector and tensor unparticle's two point functions are

$$\langle 0 | \mathcal{O}_{\mathcal{U}}^{\mu}(x) \mathcal{O}_{\mathcal{U}}^{\nu\dagger}(0) | 0 \rangle = A_{d_{\mathcal{U}}} \int \frac{d^4 P}{(2\pi)^4} e^{-iP \cdot x} \theta(P^0) \theta(P^2) (P^2)^{d_{\mathcal{U}}-2} \pi^{\mu\nu}(P) \quad (2.28)$$

$$\langle 0 | \mathcal{O}_{\mathcal{U}}^{\mu\nu}(x) \mathcal{O}_{\mathcal{U}}^{\rho\sigma\dagger}(0) | 0 \rangle = A_{d_{\mathcal{U}}} \int \frac{d^4 P}{(2\pi)^4} e^{-iP \cdot x} \theta(P^0) \theta(P^2) (P^2)^{d_{\mathcal{U}}-2} T^{\mu\nu,\rho\sigma}(P) \quad (2.29)$$

where,

$$\pi^{\mu\nu}(P) = -g^{\mu\nu} + \frac{P^{\mu} P^{\nu}}{P^2} \quad (2.30)$$

$$T^{\mu\nu,\rho\sigma}(P) = \frac{1}{2} \left\{ \pi^{\mu\rho}(P) \pi^{\nu\sigma}(P) + \pi^{\mu\sigma}(P) \pi^{\nu\rho}(P) - \frac{2}{3} \pi^{\mu\nu}(P) \pi^{\rho\sigma}(P) \right\}. \quad (2.31)$$

The propagators for vector and tensor operators are

$$\left[\Delta_F(P^2)\right]_{\mu\nu} = \frac{A_{d_U}}{2 \sin(d_U \pi)} (-P^2)^{d_U-2} \pi_{\mu\nu}(P) \quad (2.32)$$

$$\left[\Delta_F(P^2)\right]_{\mu\nu,\rho\sigma} = \frac{A_{d_U}}{2 \sin(d_U \pi)} (-P^2)^{d_U-2} T_{\mu\nu,\rho\sigma}(P). \quad (2.33)$$

All unparticle propagators are taken to be hermitian and transverse. Tensor unparticle propagator is also taken to be traceless. The constraints on vector and tensor unparticle dimension d_U are [11]:

- Lower bounds: $d_U > 3$ and $d_U > 4$ for vector and tensor unparticle respectively imposed by unitarity.
- Upper bounds: To set an upper limit on d_U for vector and tensor unparticles is problematic.

Therefore our study will be mainly focused on scalar unparticles. Nevertheless, for completeness of our search we will repeat the analysis done with scalar unparticles for tensor unparticles as well.

2.5 Effective interactions [10]

General unparticle coupling to the SM

The unparticle is coupled to the SM by terms of the form $O_{SM}O_{CFT}$, where O_{CFT} can be scalar, vector or tensor operator. The interactions depend on the dimension of the unparticle operator and whether it is scalar, vector or tensor. This is a list of some of the effective operators which describe how unparticle interacts with SM fields at low energy:

Spin-0:

$$\lambda_0 \frac{1}{\Lambda_U^{d_U-1}} \bar{f} f O_U, \quad \lambda_0 \frac{1}{\Lambda_U^{d_U-1}} \bar{f} i \gamma^5 f O_U, \quad \lambda_0 \frac{1}{\Lambda_U^{d_U}} G_{\alpha\beta} G^{\alpha\beta} O_U \quad (2.34)$$

Spin-1:

$$\lambda_1 \frac{1}{\Lambda_U^{d_U-1}} \bar{f} \gamma_\mu f O_U^\mu, \quad \lambda_1 \frac{1}{\Lambda_U^{d_U-1}} \bar{f} \gamma_\mu \gamma^5 f O_U^\mu \quad (2.35)$$

Spin-2:

$$-\frac{1}{4}\lambda_2\frac{1}{\Lambda_{\mathcal{U}}^{d_{\mathcal{U}}}}\bar{\psi}i(\gamma_{\mu}\overleftrightarrow{\mathbf{D}}_{\nu}+\gamma_{\nu}\overleftrightarrow{\mathbf{D}}_{\mu})\psi O_{\mathcal{U}}^{\mu\nu}, \quad \lambda_2\frac{1}{\Lambda_{\mathcal{U}}^{d_{\mathcal{U}}}}G_{\mu\alpha}G_{\nu}^{\alpha}O_{\mathcal{U}}^{\mu\nu} \quad (2.36)$$

Here $O_{\mathcal{U}}$, $O_{\mathcal{U}}^{\mu}$ and $O_{\mathcal{U}}^{\mu\nu}$ stand for scalar, vector and tensor unparticle operators, f is standard model fermion, ψ is standard model fermion doublet or singlet, λ_i are dimensionless effective couplings $C_{O_{\mathcal{U}}^i}\Lambda_{\mathcal{U}}^{d_{\mathcal{B}Z}}/M_{\mathcal{U}}^{d_{SM}+d_{\mathcal{B}Z}-4}$, \mathbf{D} is a gauge covariant derivative.

Virtual exchange of unparticle

Virtual exchange of spin-1 unparticle between two fermionic currents corresponding to $O_{\mathcal{U}}^{\mu}$ leads to 4-fermion interactions

$$\mathcal{M}_1^{4f} = \lambda_1^2 Z_{d_{\mathcal{U}}} \frac{1}{\Lambda_{\mathcal{U}}^2} \left(-\frac{P_{\mathcal{U}}^2}{\Lambda_{\mathcal{U}}^2} \right)^{d_{\mathcal{U}}-2} (\bar{f}_2 \gamma_{\mu} f_1) (\bar{f}_4 \gamma^{\mu} f_3). \quad (2.37)$$

There are two important characteristics of this amplitude which give rise to interesting features of unparticles. The first one is the (-) sign in front of $P_{\mathcal{U}}^2$ in Equation 2.37 that gives a phase factor $\exp(-i\pi d_{\mathcal{U}})$ for time-like momentum $P_{\mathcal{U}}^2 > 0$, which leads to nontrivial interference patterns with SM amplitudes. The second feature is that the amplitude scales as $(s/\Lambda_{\mathcal{U}}^2)^{d_{\mathcal{U}}-1}$, which for different values of the scaling dimension $d_{\mathcal{U}}$ can lead to various forms of the unparticle amplitude. For $d_{\mathcal{U}} = 1$ the amplitude is like that of photon exchange. For $d_{\mathcal{U}} = 2$ the amplitude reduces to the conventional 4-fermion interaction. For $d_{\mathcal{U}} = 3/2$, the amplitude scales as $\sqrt{s}/\Lambda_{\mathcal{U}}$ and has an unusual behavior. If $d_{\mathcal{U}} = 3$ the amplitude becomes $(s/\Lambda_{\mathcal{U}}^2)^2$, which resembles the exchange of Kaluza-Klein (KK) tower of gravitons.

On the other hand, the virtual exchange of spin-2 unparticle between two fermionic currents corresponding to $O_{\mathcal{U}}^{\mu\nu}$ leads to the following 4-fermion interaction

$$\begin{aligned} \mathcal{M}_2^{4f} &= -\frac{1}{8}\lambda_2^2 Z_{d_{\mathcal{U}}} \frac{1}{\Lambda_{\mathcal{U}}^4} \left(-\frac{P_{\mathcal{U}}^2}{\Lambda_{\mathcal{U}}^2} \right)^{d_{\mathcal{U}}-2} (\bar{f}_2 \gamma^{\mu} f_1) (\bar{f}_4 \gamma^{\nu} f_3) \\ &\quad \times \left[(p_1 + p_2) \cdot (p_3 + p_4) g_{\mu\nu} + (p_1 + p_2)_{\nu} (p_3 + p_4)_{\mu} \right]. \end{aligned} \quad (2.38)$$

In this case the amplitude is further suppressed by $(s/\Lambda_{\mathcal{U}})^2$ relative to the one for spin-1 unparticle and is similar to spin-2 graviton exchange ($d_{\mathcal{U}} = 2$). Therefore the cross section for spin-2 unparticle is identical to the graviton's cross section with the following translation of parameters

$$d_{\mathcal{U}} = \frac{n}{2} + 1 \quad (2.39)$$

where n is the number of Large Extra Dimension (LED) that can take only integer values with respect to $d_{\mathcal{U}}$ which can take also non-integer values. Therefore unparticle models can be considered as a slight generalization of an extra dimension model. Based on that, in our analysis where we search for unparticles in diphoton final state, we use many common tools which have been developed by analysis searching for LED in diphoton final state. This will be discussed in details in Chapter 4.

Now, knowing how unparticles interact, we will give some examples of unparticle production via direct unparticle emission and indirect interference effect or also known as virtual unparticle exchange.

2.6 Direct production of unparticles

The main signature of the real emission of unparticles includes missing energy and momentum. Some of the processes involving real unparticle emission are:

1. Mono-photon events:
 - $e^- e^+ \rightarrow \gamma \mathcal{U}, Z \mathcal{U}$ [12]
 - Quarkonia $\rightarrow \gamma \mathcal{U}$ [13]
 - Higgs $\rightarrow \gamma \mathcal{U}$ [14]
 - $Z \rightarrow \gamma \mathcal{U}$ [13], [15]

The energy distributions of all these processes are very sensitive to various choices of the scale dimension $d_{\mathcal{U}}$, both for vector and tensor unparticle production. The non-integral value of $d_{\mathcal{U}}$ results in a peculiar form of the recoil mass distributions and the photon energy.

2. Monojet production [16]:

- $gg \rightarrow g \mathcal{U}$
- $q\bar{q} \rightarrow g \mathcal{U}$

- $qg \rightarrow q\mathcal{U}$
- $\bar{q}g \rightarrow \bar{q}\mathcal{U}$

In comparison with mono-photon/mono-Z plus unparticle production, the monojet plus unparticle signal will be very difficult to analyze at LHC [10]. There is only one jet at the final state which means that not many observables can be reconstructed. The matrix elements of the cross section for these processes strongly depend on the scaling dimension $d_{\mathcal{U}}$ and their effect is completely washed out due to parton smearing effects. Extended analysis that compare unparticle and ADD graviton emission in monojet E_T spectra was done in [16]. It has been concluded that while the unparticle predictions themselves are difficult to distinguish, they are all easily differentiable from those of the ADD model. Figure 2.1 shows comparison of the monojet E_T distribution in the ADD model with scalar and vector unparticle's E_T distributions.

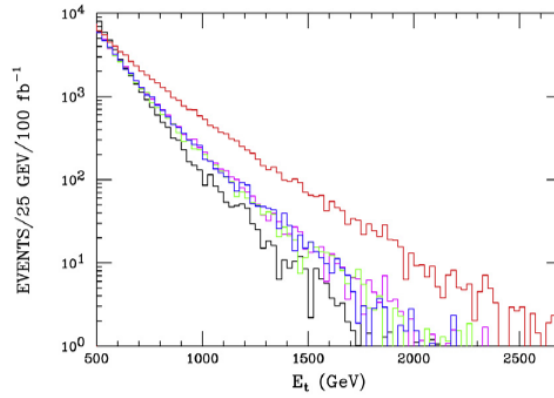


Figure 2.1: Comparison of the prediction for the monojet E_T distribution in the ADD model with $M_D = 4$ TeV and $\delta = 2$ (red) with scalar (green and magenta) and vector (blue) unparticle for chosen unparticle parameters. SM background is shown in black [16].

3. Z decay [12]: $Z \rightarrow f\bar{f}\mathcal{U}$

This process, in analogy with the mono-photon events in the final state, is very sensitive on the scaling dimension $d_{\mathcal{U}}$ of the unparticle operators. When $d_{\mathcal{U}} \rightarrow 1$ the results approach the SM process $\gamma^* \rightarrow q\bar{q}g^*$.

4. Top quark decay [7]: $t \rightarrow b\mathcal{U}$

When $d_{\mathcal{U}} \rightarrow 1$ is recovered the SM two body decay kinematics. However when $d_{\mathcal{U}} > 1$, there is a continuum of energies which shows that unparticle does not have a definite

mass.

2.7 Virtual exchange of unparticles

The virtual exchange of unparticles is another indirect way to search for their existence. They were studied in great detail in [10], [12] and [17]. Some of the processes that include virtual unparticle exchange are Drell-Yan $gg, q\bar{q} \rightarrow \mathcal{U} \rightarrow e^+e^-$ and fermion pair production $e^+e^- \rightarrow \mathcal{U} \rightarrow \mu^+\mu^-$.

The unparticle propagator has a very complicated nature because of the non-integral values of the scaling dimension $d_{\mathcal{U}}$. This can give rise to interference effects among the amplitudes of the unparticle and SM fields. For $e^+e^- \rightarrow \mathcal{U} \rightarrow \mu^+\mu^-$ it has been shown that these interference effects depend on the scaling dimension $d_{\mathcal{U}}$ and the forward-backward asymmetry, and are most observable at the Z pole. Similar interference effects has been observed for Drell-Yan process $gg, q\bar{q} \rightarrow \mathcal{U} \rightarrow e^+e^-$ in [10].

The diphoton production mediated via virtual unparticles gives another example of interference effects of unparticles with SM fields. These processes has been studied both in e^+e^- and hadronic colliders. In e^+e^- colliders [10], it was argued that the diphotons coming from unparticles can be discriminated more easily from the SM diphotons using angular distribution. In this case, the SM angular distribution is very forward with majority of its cross section at $|\cos\theta_\gamma|$ close to 1 with respect to the unparticle one. This distribution was also shown to be strongly dependent on the unparticle scale dimension $d_{\mathcal{U}}$. In this thesis, we will focus our search to detect unparticles in diphoton production in the hadronic collider LHC. We will show how unparticles can be distinguished from the SM diphoton production using different kinematical distributions like invariant mass, angle θ and rapidity.

On the other hand, virtual unparticles can also interact among themselves. This is called self-interaction and has the form of $pp \rightarrow \mathcal{U} \rightarrow \mathcal{U} \dots \mathcal{U}$ that leads to two or more unparticles in the final state. In SM processes the addition of every high p_T particle in the final state leads to decrease of the production rate. However, creation of additional high p_T unparticles does not suppress the rate [18]. The cross section of such a process can be suppressed mainly by conversion back of the unparticles to visible particles.

The self-interaction of unparticles produced in proton proton collisions $pp \rightarrow \mathcal{U} \rightarrow \mathcal{U}\mathcal{U} \rightarrow$ can lead to the following final states: $\gamma\gamma\gamma\gamma$, $\gamma\gamma ZZ$, $ZZZZ$, $\gamma\gamma l^+ l^-$, $ZZ l^+ l^-$ and $4l$.

In [19] further were developed techniques for studying n unparticle self-interactions. It has been argued that just like the interactions between particles produce new particles, the unparticle self-interactions cause the production of different kind of unparticles. For that purpose a simplified Sommerfield model of the Banks-Zaks sector is being used.

2.8 Unparticle decay [20]

In Section 2.6 we discussed unparticles that escape undetected from the detector and manifest themselves as missing energy. In fact, unparticles can decay back to SM particles just like normal resonances. Therefore, in general, unparticles may not be characterized by missing energy signals but instead decay to some known particles. Depending on the unparticle's lifetime they can show their existence by various ways:

- Short lifetime: Prompt decays;
- Unparticle travel a macroscopic distance before decaying: Delayed jets / photons;
- Long lifetime: Monojets and missing energy.

To see how unparticle decay, we sum the corrections from all loop diagrams. The unparticle is regarded as a sum over several particle propagators and the full unparticle propagator is given by

$$\int e^{ipx} \langle 0 | T(O_{\mathcal{U}}(x) O_{\mathcal{U}}(0)) | 0 \rangle d^4x \equiv \frac{iB_{d\mathcal{U}}}{(p^2 - \mu^2)^{2-d} - B_{d\mathcal{U}} \Sigma(p^2)} \quad (2.40)$$

where the loop diagram is pure imaginary $\Sigma(p^2) = -\Sigma_I(p^2)$ and is proportional to the width. The mass gap μ is a scale in the CFT that is been introduced after the coupling of unparticle to Higgs field [20]. $B_{d\mathcal{U}}$ is given by

$$B_{d\mathcal{U}} \equiv A_{d\mathcal{U}} \frac{(e^{i\pi})^{d\mathcal{U}-2}}{2 \sin d\mathcal{U}\pi} \quad (2.41)$$

with $A_{d\mathcal{U}}$ defined in Equation 3.5.

If the above assumptions for the propagator are correct, then the unparticle is allowed to decay to SM particles. Its decay width $\Gamma(M)$, which is a sum over the infinite set of resonances with mass M , required by unitarity is

$$\Gamma(M) = \frac{\sum_I(M^2)}{(2-d)M} (M^2 - \mu^2)^{d-1} \frac{A_d}{2} \cot(\pi d). \quad (2.42)$$

Therefore unparticle's lifetime is $\Gamma^{-1}(M)$.

Suppose the unparticle has the couplings

$$L_{int} = \frac{O_{\mathcal{U}} F_{\mu\nu} F^{\mu\nu}}{\Lambda_F^{d_{\mathcal{U}}}} + \frac{O_{\mathcal{U}} G_{\mu\nu} G^{\mu\nu}}{\Lambda_G^{d_{\mathcal{U}}}} \quad (2.43)$$

where $F_{\mu\nu}$, $G_{\mu\nu}$ are the electromagnetic and color field strength, and Λ_F , Λ_G are scale couplings. Unparticles can be produced through processes like $gg \rightarrow gO_{\mathcal{U}}$ that lead to monojet production when unparticle's lifetime is long enough. Subsequently, they can decay either to gluons or photons: $O_{\mathcal{U}} \rightarrow gg$ and $O_{\mathcal{U}} \rightarrow \gamma\gamma$. Depending on the lifetime of unparticle, the final state can be:

- If the lifetime of unparticle is less than $100ps$ the decay is prompt. In the final state there are two photons with an extra hard jet;
- If unparticle decay outside the detector there is a monojet signal and missing energy;
- If unparticle decays before exiting the detector there are photons or gluons which can be detected with a time delay given by the lifetime of the unparticle. Because the unparticle will be strongly boosted, the decay products will be collinear and appear as single photon/jet accompanied by hard jet.

Figure 2.2 shows the number of events of each type of decays as a function of the mass gap μ for $d_{\mathcal{U}} = 1.1$ and $\Lambda_{\mathcal{U}} = 10$ TeV. It was additionally required that the jet has energy more than 100 GeV, the detector is ~ 1 m in size and delays of 100 ps can be measured.

The conclusion from Figure 2.2 is that:

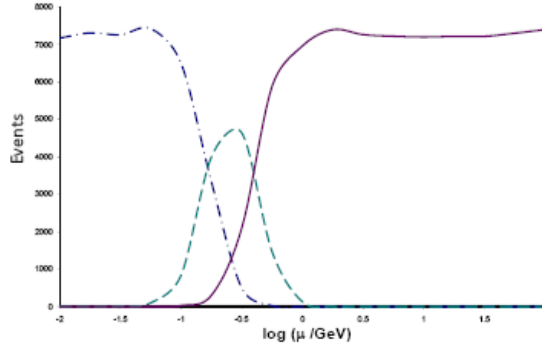


Figure 2.2: Number of events with $10fb^{-1}$ as a function of the mass gap μ . The solid (red) line corresponds to prompt events, the dot-dashed (blue) line corresponds to monojet events and the dashed (green) line corresponds to delayed events [20].

- For $\mu > 10$ GeV, there are only prompt events;
- If $\mu < 100$ MeV, there is significant number of monojets;
- If $\mu \sim 1$ GeV, large number of delayed events.

2.9 Unparticle mass gap

A comparison between all the unparticle production processes shown till now leads to the following conclusions. A real unparticle production manifests itself as missing energy and momentum. A virtual unparticle production is a very rare process which leads to interference effects with SM processes. A multi-unparticle production which occurs when there is self-interaction among unparticles, leads to spectacular signals in the colliders. All of these processes are distinguishable from other physics processes through bizarre kinematic properties of the unparticles.

Till now we assumed that below some scale Λ_U the unparticle sector is scale invariant. However it might not be correct. In [22] and [23] it has been suggested that scale invariance may not be an exact symmetry at low energy.

When scalar unparticle operator couple to the SM Higgs field, it can break the scale invariance by introducing a scale μ . It means that unparticle physics is only possible in a conformal

window which leads subsequently to a modification of the unparticle propagator and to many new implications as existence of unresonances [24], Higgs physics [25] and colored unparticles [26].

Now we will argue that the interactions between unparticles and SM sector induce a mass gap, μ . The mass gap is a scale at which conformal theory for unparticles is broken. This can happen due to the coupling of unparticles to the Higgs sector which takes the form

$$C\mathcal{U}\frac{\Lambda_{\mathcal{U}}^{d_{\mathcal{BZ}}-d_{\mathcal{U}}}}{M_{\mathcal{U}}^{d_{\mathcal{BZ}}-2}}|H|^2\mathcal{O}_{\mathcal{U}}. \quad (2.44)$$

When the Higgs gets a vacuum expectation value (vev), the Higgs operator breaks the conformal invariance of the hidden sector and introduces a scale μ into the CFT. At this scale, the unparticle sector flows away from its fixed point and the theory becomes nonconformal. The breaking scale, μ , at which this happens is found to be sufficiently low and has the form

$$\mu^{4-d_{\mathcal{U}}} = \left(\frac{\Lambda_{\mathcal{U}}}{M_{\mathcal{U}}}\right)^{d_{\mathcal{BZ}}-d_{\mathcal{U}}} M_{\mathcal{U}}^{2-d_{\mathcal{U}}} v^2 \quad (2.45)$$

where v is the Higgs vev. Below this scale the unparticle sector becomes traditional particle sector.

2.10 Unparticle astrophysics and cosmology [27]

There are many bounds on unparticles imposed by SM processes [13] however the most stringent ones come from astrophysics and cosmology. These constraints impose that unparticles can not be observed at high energy colliders. However all these constraints can be avoided if there exists an unparticle mass gap which makes possible unparticle physics only in a conformal window as discussed in Section 2.9.

Assuming there is no unparticle mass gap and for the completeness of our study, in this chapter we show the implication of astrophysics and cosmology on unparticle production and the possible constraints on its parameters [28], [29], [27].

2.10.1 Limits from astrophysics

Astrophysical limits on unparticle production include constraints from 5th force experiment and the energy loss from red giants and supernova SN1987A. Table 2.1 lists the lower bounds on $M_{\mathcal{U}}$ from energy loss from supernova SN 1987A, red giant and 5th force experiment.

Table 2.1: Constraints on unparticles from energy loss from supernova SN 1987A, red giant and 5th force experiment [27].

$M_{\mathcal{U}}$	$d_{\mathcal{U}} = 1$	$d_{\mathcal{U}} = 4/3$	$d_{\mathcal{U}} = 5/3$	$d_{\mathcal{U}} = 2$
<i>5thForce</i>	$3.8 \times 10^{14} \text{ GeV}$	$1.8 \times 10^{10} \text{ GeV}$	$3.4 \times 10^7 \text{ GeV}$	$6.7 \times 10^4 \text{ GeV}$
<i>Redgiant</i>	$2.2 \times 10^{10} \text{ GeV}$	$4.2 \times 10^8 \text{ GeV}$	$1.4 \times 10^7 \text{ GeV}$	$5.1 \times 10^5 \text{ GeV}$
<i>SN1987A</i>	$3.2 \times 10^7 \text{ GeV}$	$3.6 \times 10^6 \text{ GeV}$	$4.5 \times 10^5 \text{ GeV}$	$5.5 \times 10^4 \text{ GeV}$

Constraints on the messenger's mass $M_{\mathcal{U}}$ from supernova SN 1987A were imposed by the emission of unparticles via nucleon bremsstrahlung ($n + n \rightarrow n + n + \mathcal{U}$). In the case of red giant star, the constraints were imposed by production of unparticles via bremsstrahlung ($e + H^+ \rightarrow e + H^+ + \mathcal{U}$), where H^+ is hydrogen, and Compton process ($\gamma + e \rightarrow e + \mathcal{U}$).

2.10.2 Constraints from cosmology

Cosmology imposes limits on the unparticle parameters based on the effect of Big-Bang Nucleosynthesis (BBN) of the unparticle energy density produced by thermal SM particles. If unparticle density is stable at the time of BBN, we can put constraints on the messenger mass $M_{\mathcal{U}}$ and temperature T of the SM. It was found that the temperature T of the SM particles depends on the mass the messenger particle $M_{\mathcal{U}}$ in the following way

$$T \lesssim 1.8 \left(\frac{M_{\mathcal{U}}}{100 \text{ TeV}} \right)^{6/5}. \quad (2.46)$$

For $M_{\mathcal{U}}$ near its lower bound the temperature of the SM sector has upper bound 1 – 10 TeV. When $1.1 \lesssim d_{\mathcal{U}} \lesssim 2$, $2 \lesssim d_{BZ} \lesssim 4$ and $\Lambda_{\mathcal{U}} \gtrsim 1 \text{ TeV}$ the messenger mass was found to be $M_{\mathcal{U}} \gtrsim 20 - 2400 \text{ TeV}$.

2.11 Unparticle dark matter [30]

Majority of the energy in our universe is carried by dark matter and dark energy. Since there is no suitable candidate for dark matter in the SM, a search for a new physics beyond the SM is necessary. It was suggested that unparticles can be this appropriate dark matter candidate.

In general the relic abundance of the dark matter is obtained by solving Boltzmann equation

$$\frac{dY}{dx} = -\frac{\langle\sigma v\rangle}{Hx} s(Y^2 - Y_{eq}^2) \quad (2.47)$$

where,

- Y is the ratio of the dark matter density to the entropy density of the universe;
- H is the Hubble parameter;
- $x = m_{\mathcal{U}}/T$ with $m_{\mathcal{U}}$ unparticle mass and T the temperature of the universe;
- $\langle\sigma v\rangle$ is the averaged annihilation cross section;
- Y_{eq} is the abundance of dark matter at equilibrium, $Y_{eq} = (0.434/g^*)x^{3/2}e^{-x}$ with $g^* = 86.25$.

The solution of this equation gives the present abundance of dark matter which is also approximately given by the following equation

$$\Omega h^2 = \frac{1.07 \times 10^9 x_f \text{GeV}^{-1}}{\sqrt{g^*} m_{PL} \langle\sigma v\rangle} \quad (2.48)$$

where x_f is the freeze-out temperature of the dark matter and $m_{PL} = 1.22 \times 10^{19}$ GeV is the Planck mass .

We are interested in the interaction between unparticle and SM Higgs doublet, because this is the most important process at low energies. We also assume that unparticle is massless but it obtains mass through its interaction with Higgs doublet and become a dark matter candidate.

The annihilation cross section, σv , can be calculated considering all the possible processes through which unparticle can annihilate $\mathcal{U}\mathcal{U} \rightarrow h \rightarrow W^+W^-, ZZ, f\bar{f}$. Afterwards, the

value of σv is substituted in Equation 2.48 to find the relic abundance Ωh^2 for different Higgs masses.

Figure 2.3 illustrates the relic abundance, Ωh^2 , of the unparticle dark matter as a function of Higgs boson mass m_h . Subsequently, the relic abundance of the unparticle dark matter is shown in Figure 2.4 in (m_U, m_h) plane.

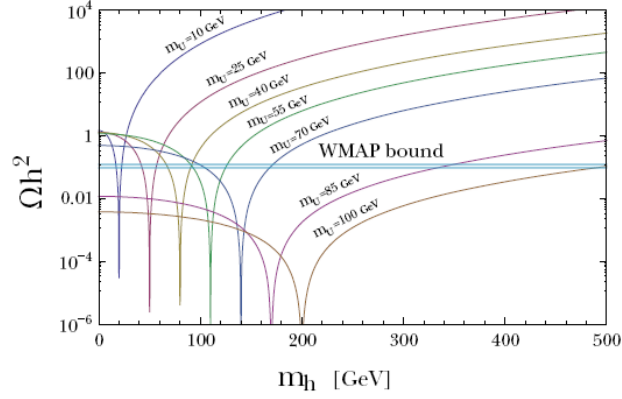


Figure 2.3: The relic abundance of the unparticle dark matter as a function of the Higgs boson mass for given unparticle masses, together with constraint on the relic abundance from WMAP measurement [30].

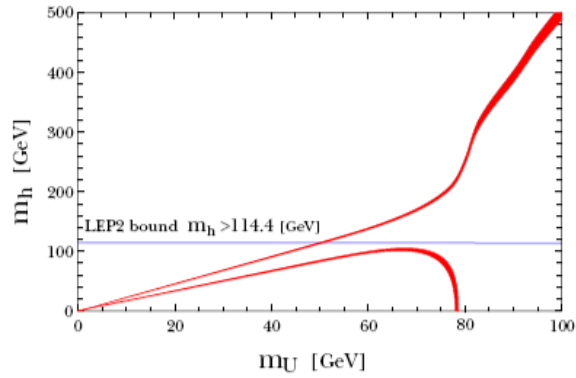


Figure 2.4: The relic abundance of the unparticle dark matter. The shaded area is the allowed region for the WMAP measurements at 2σ confidence level [30].

Considering the existing constraint on the relic abundance Ωh^2 from WMAP satellite to be

$$0.096 \leq \Omega h^2 \leq 0.122 \quad (2.49)$$

it can be concluded that the unparticle mass, m_U , should be around electroweak scale.

CHAPTER 3

THE LHC AND THE CMS EXPERIMENT

3.1 The LHC

The Large Hadron Collider (LHC) [31] has been constructed in the already existing LEP tunnel 100 m underground which straddles the Swiss and French borders and has circumference of 27 km. The LHC is primarily designed to collide two beams of protons, though heavy ions will also be collided for approximately one month of every year. Proton (ion) beams with energy of 7 TeV will be collided by magnetic fields of up to 8.33 Tesla at a design luminosity of $L = 10^{34} \text{ cm}^{-2} \text{ s}^{-1}$.

In the last twenty years, the LEP and Tevatron experiments have confirmed many of the theoretical predictions of the Standard Model. LEP measured the masses and properties of the W^\pm and Z bosons and Tevatron discovered the top quark and measured its mass to a precision of 1 %. However there are still many unanswered questions like origin of mass, the matter antimatter asymmetry and the unification of the four fundamental forces.

The LHC machine is designed for discovery and to study physics at TeV energy scale. For instance, Higgs boson is the only particle in the SM, if it exist, that still has not been discovered. The LHC will search for the Higgs boson, up to scales of 1 TeV.

The layout of the LHC is shown in Figure 3.1 and some important design parameters of LHC are given in Table 3.1.

LHC is designed to collide protons. They were chosen over leptons, in order to reach higher energies. Accelerating either electrons or protons in a magnetic field is accompanied by energy loss through synchrotron radiation. This energy loss is proportional to m^{-4} , where m

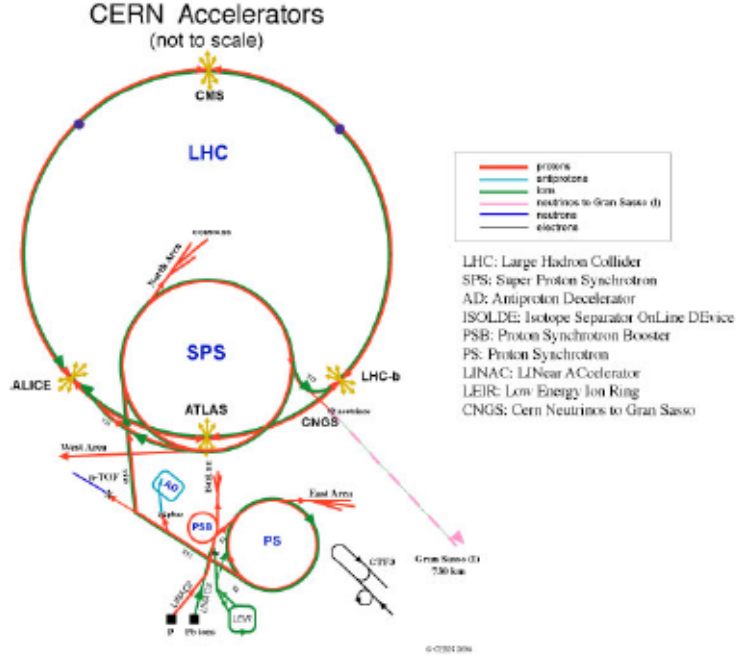


Figure 3.1: The layout of the Large Hadron Collider.

is the mass of the particle. Therefore the energy loss is much smaller for heavier protons.

Before entering the LHC ring, protons are prepared through a series of systems that successively drive up protons energy levels in order to be reached the injection energy for the LHC. First protons are accelerated in Linear Accelerator (LINAC) to energies up to 50 MeV. The particles are then injected into Proton Synchrotron Booster (PSB) to reach energies up to 1.4 GeV and later into the Proton Synchrotron Ring (PSR) to 26 GeV. At the end particles enter Super Proton Synchrotron (SPS) where their energy is increased up to 450 GeV. Afterwords the protons are injected into the LHC ring and accelerated there many times in order to reach the designed energy of 7 TeV. The overall time for the protons to be accelerated in the subsystems is approximately 16 minutes. After that the time to reach the collision energy of 7 TeV counted from the time when the particles were injected into the LHC ring is approximately 20 minutes. The total time for one turnaround at the ring is about 70 minutes. The integrated luminosity for one run can be then calculated using the formula

$$L_{int} = L_0 \tau_L \left[1 - e^{-T_{run}/\tau_L} \right], \quad (3.1)$$

Table 3.1: Design parameters of the LHC.

Particle	Detection method
Beam particles	pp
Injection energy	0.45 TeV
Beam energy	7 TeV
Number of dipole magnets	1232
Luminosity	$10^{34} cm^{-2} s^{-1}$
Particles per bunch	1.1×10^{11}
Number of bunches	2808
Bunch spacing	25 ns

where L_0 is the peak luminosity value, τ_L is the luminosity lifetime, T_{run} is the total length of the luminosity run. For 1 year run it has been calculated that the integrated luminosity is around $100 fb^{-1}$.

The LHC will resume operation in November 2009 initially at 7 TeV center of mass energy and once significant amount of test data has been gathered will be increased to 10 TeV. At the end of 2010 the LHC will be shut down and work will begin on it to allow it to operate at 14 TeV center of mass energy.

This work is performed to do analysis at 10 TeV center of mass energy and data sample corresponding to integrated luminosity of $100 pb^{-1}$, expected to be collected at the first LHC run.

Superconducting dipole magnets are used to deflect the protons around the ring and quadrapole magnets are used to focus the two beams together.

There are four main experiments at LHC: ALICE, ATLAS, CMS and LHCb. ATLAS (A Toroidal LHC ApparatuS) and CMS (Compact Muon Solenoid) are general purpose detectors that are designed to search for new particles. ALICE (A Large Ion Collider Experiment) is designed to study heavy ion collisions and in particular quark-gluon plasma, which is the state of matter shortly after the Big Bang. LHCb is designed to study the CP violation by measuring the properties of b-hadrons.

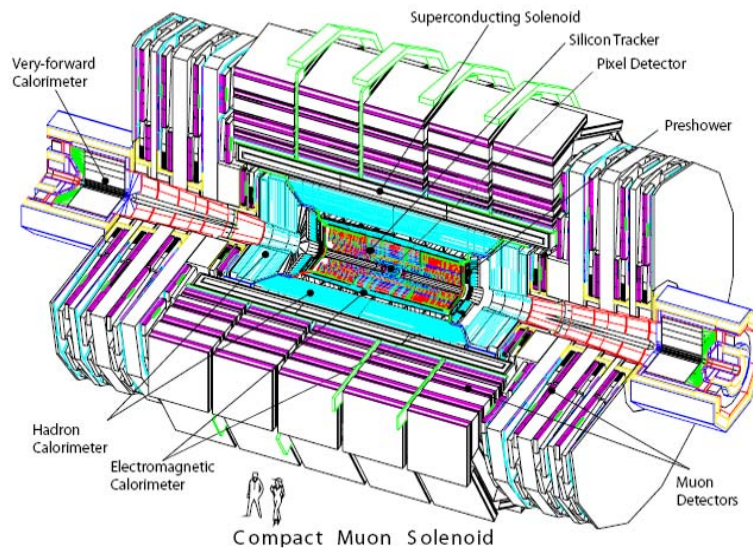


Figure 3.2: A perspective view of the CMS detector [32].

3.2 CMS [32]

The Compact Muon Solenoid (CMS) experiment is one of the four detectors that have been designed to exploit the physics opportunities presented by LHC. The overall dimensions are a length of 21.6 m, a diameter of 14.6 m and a total weight of 12500 tons. Every 25 ns, beam crossing occurs in the CMS detector at a rate of 40 MHz which gives 1 billion events occurring in the CMS detector every second, which all need to be analyzed in extremely short time. In order to extract physics from these interactions it is important to have fast electronics and very good resolution. Because these events occur very quickly, a large amount of disk space is necessary, thus it is better to store only the "interesting" events by precise triggering.

The CMS detector has a barrel design with two endcaps covering the largest possible angular range. CMS is designed to take measurement of every known particle, in order to search for new particles. Each subdetector of CMS can identify and measure different set of particles which affects the usage of various technologies for each of the subdetectors. The main distinguishing features of CMS are a superconducting solenoid with 3.8 Tesla magnetic field, a full-silicon-based inner tracking system and a homogeneous scintillating-crystals-based electromagnetic calorimeter. The CMS detector was built to provide mainly good muon detection

and resolution. The overall view of CMS detector is shown in Figure 3.2.

3.2.1 Coordinate system

The CMS detector is located north of the LHC center and the origin of the CMS coordinate system is the CMS collision point. The x -axis is horizontal, pointing south to the LHC center. The y -axis is vertical, pointing upwards. The z -axis is horizontal pointing west. The azimuthal angle ϕ is measured in the $x - y$ plane and the polar angle θ is measured from the z -axis which is orthogonal to the $x - y$ plane.

The relativistic approximation to the true rapidity y , is given by the pseudorapidity, $\eta = -\ln[\tan(\theta/2)]$. The components of energy and momentum measured to the beam direction are denoted E_T and p_T respectively and any imbalance in the vector sum of E_T is denoted E_T^{miss} .

3.2.2 Superconducting magnet

CMS has a large superconducting solenoid magnet that will provide a strong magnetic field of 3.8 T. In this field charged particles can be bent and their trajectories can be measured in order to find their momenta. The solenoid magnet is 13 m long and has inner diameter of 6 m and consists of a superconducting coil inside a vacuum tank, a magnet yoke (barrel and endcap) and ancillaries such as cryogenics and power supplies. At full current the total energy stored in the magnet is 2.66 GJ.

3.2.3 Inner tracking system

The tracker has cylindrical shape with length of 5.8 m and diameter of 2.5 m, and consists of 1440 pixel and 15148 strip detector modules. Its main purpose is to measure momentum and impact parameter of charged particles with minimum multiple scattering. The tracker can reconstruct the paths of high-energy muons, electrons and hadrons as well as tracks coming from the decay of short-lived particles like b-quarks in the range $|\eta| < 2.5$. It is also designed to identify tracks coming from displaced vertices. The path of the particles is determined by finding their position at a number of key points. Each measurement of the position is accurate to $10 \mu\text{m}$ and is performed in such a way as to disturb the particle as little as possible.

Subsequently the path is used to find the particle's momentum p using the curvature ρ of its trajectory. To minimize multiple scattering, we want the tracker to contain as little material as possible. Silicon was chosen as the main sensor material for its fast response and small strip pitch. The CMS tracker is composed of:

1. **Inner silicon pixel detector.** The pixel detector consists of three barrel layers at radii between 4.4 cm and 10.2 cm. It covers pseudorapidity range of $-2.5 < \eta < 2.5$ and is dealing with the highest intensity of particles by measuring the impact parameter of charged particle tracks and the position of secondary vertices.
2. **Outer silicon microstrip detector.** The strip tracker surrounds the pixel detector and is placed in ten layers in barrel, extending outwards to a radius of 1.1 m and deals with medium to low track multiplicities.
3. **Endcaps.** Each system is completed by endcaps which consist of 2 discs in the pixel detector and 3 plus 9 discs in the strip tracker on each side of the barrel, extending the acceptance of the tracker up to a pseudorapidity of $|\eta| < 2.5$.

The whole tracker will operate at a temperature below -10 C° . When particles travel through the tracker, the pixels and microstrips produce electric signals that are amplified and detected.

3.2.4 Electromagnetic calorimeter

The electromagnetic calorimeter (ECAL) is designed to measure photons and electrons. In its designed specification, the most important feature is the best possible energy resolution. This is crucial for the reconstruction of the invariant mass of two photons for $Higgs \rightarrow \gamma\gamma$ channel for Higgs mass $< 150\text{ GeV}$.

The ECAL consists of a central barrel region, which covers the pseudorapidity range $|\eta| < 1.479$ and two endcap regions, which cover $1.479 < |\eta| < 3.0$. There are 61200 lead tungstate (PbWO_4) crystals in the central barrel part and 7324 crystals in each endcap. Lead tungstate was chosen as the crystal material because of its high density (8.28 g/cm^3) which leads to short radiation length ($X_0 = 0.89\text{ cm}$) and small Moliere radius (2.2 cm). This allows a very compact calorimeter system which reduces the effect of the magnetic field on the electrons

and reduces the cost of the detector. Figure 3.3 shows layout of the ECAL with position of the crystal modules.

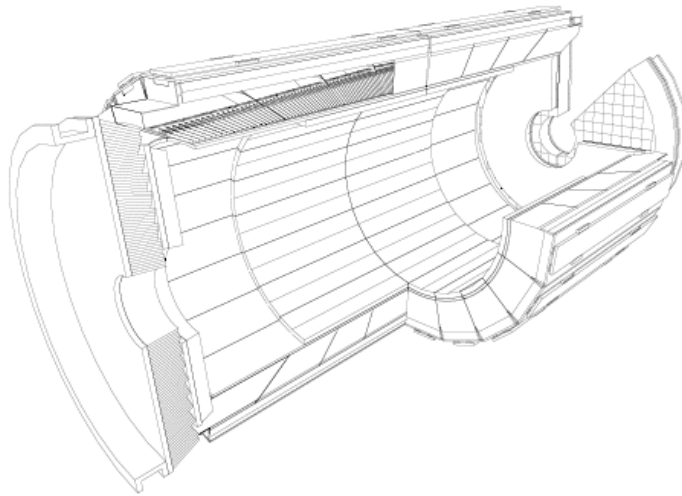


Figure 3.3: Layout of the CMS ECAL showing the arrangement of crystal modules, super-modules and endcaps [32].

When electrons and photons pass through tungstate crystals, they scintillate in proportion to the particle's energy, a light shower is created by bremsstrahlung and pair production. Afterwards the scintillation light is detected by photodetectors - silicon avalanche photodiodes (APDs) in the barrel and vacuum phototriodes (VPTs) in the endcaps which are placed on the back of each of the crystals. These photodetectors need to be fast and radiation tolerant to be able to operate in 4 T magnetic field.

After passing through the photodetectors the scintillation light is then converted into an electrical signal which is read out by on-detector electronics. This electronics must be with high speed and precision in order to acquire the small signals of the photodetectors.

In front of the endcap ECAL is placed the preshower detector that covers a region between $1.653 < |\eta| < 2.6$. It contains two thin lead converters that initiate electromagnetic showers from incoming photons/electrons. After each of the converters there are silicon strip planes that measure the deposited energy and the transverse shower profile. The total thickness of the preshower is 20 cm. The main purpose of this detector is to enable us to distinguish between single high-energy photons and close pair of low-energy photons (π^0 decay). It also helps the identification of electrons against minimum ionizing particles and improves the position

determination of electrons and photons.

The energy resolution $\left(\frac{\sigma}{E}\right)$ for ECAL is parametrized as given in Equation 3.2, where S is stochastic term, N is noise term and C is constant term

$$\left(\frac{\sigma}{E}\right)^2 = \left(\frac{S}{\sqrt{E}}\right)^2 + \left(\frac{N}{E}\right)^2 + C^2. \quad (3.2)$$

Basic contributions from the stochastic term are fluctuations in the lateral shower containment and from photostatistics. The contributions to constant term come from non-uniformity of the longitudinal light collection, intercalibration errors and leakage of energy from the back of the crystal. The noise term includes electronic, digitization and pileup noise.

3.2.5 Hadron calorimeter

The hadron calorimeter (HCAL) plays an essential role in the measurement of quarks, gluons and neutrinos. It is very important also for the identification and measurement of jets and missing transverse energy. The HCAL consists of central calorimeter that covers pseudorapidity range $|\eta| < 3$ and two forward hadronic calorimeters (HF) that cover up to $|\eta| < 5$.

The central calorimeter consist of hadron barrel (HB) and two endcaps (HE) which are placed completely inside the magnetic coil. HB and HE are sampling calorimeters. They consist of 5 mm absorbing plates made from brass and an active material between them. The sampling layers are made from 4 mm scintillator plastic tiles , that was chosen for its radiation hardness and long term stability. When a hadronic particle enter the HCAL it will produce a particle shower in the absorber material. This will produce scintillation light in the plastic layer. Then the light is collected by shifting fibre and carried to hybrid photodiode.

The forward calorimeter (HF) consists of steel plates instead of copper ones because of harsher radiation in the forward area. The energy is measured from the light produced in the quartz fibres. After, this light is carried to photomultipliers (HPDs) which are placed in radiation shielded areas of the calorimeter.

The outer hadron calorimeter (HO) consists of layers of scintillator tiles placed outside the HB. It is designed to sample the tails of hadronic showers which occur deep inside the calorimeter. It ensures the complete energy absorption for high energy hadronic showers.

Figure 3.4 shows the location of the different sections of HCAL.



Figure 3.4: CMS HCAL barrel in hadron calorimeter [32].

When the amount of light in a given region is summed up over many layers of tiles in depth (there are about 70000 tiles in CMS HCAL), called a tower, this total amount of light is a measure of particle's energy.

3.2.6 Muon system

The muon detecting system is the largest part of the CMS detector and the detection of muons is one of the most important tasks of the CMS, as its name suggests this. The muon detectors consist of four concentric shells interleaved with the iron return yoke plates and eight (four per side) round endcap plates. Each shell and plate is composed of twelve sectors which cover 30° in ϕ . The muon chambers are within the return yoke of the magnet which means that muon's momentum can be measured not only in the tracker but in the muon chambers as well. They are arranged in concentric cylinders around the beam line in the barrel region, and in disks perpendicular to the beam line in the endcaps. Muon chambers are shown in Figure 3.5.

The barrel ($|\eta| < 1.2$) uses Drift Tube Chambers (DTs) and Resistive Plate Chambers (RPCs). The endcap use Cathode Strip Chambers (CSCs) and RPCs and cover $|\eta| < 2.4$. This combination is used because DTs and CSCs provide accurate position measurement but have a large lag time. On the other hand RPCs have a very accurate time measurement and short re-

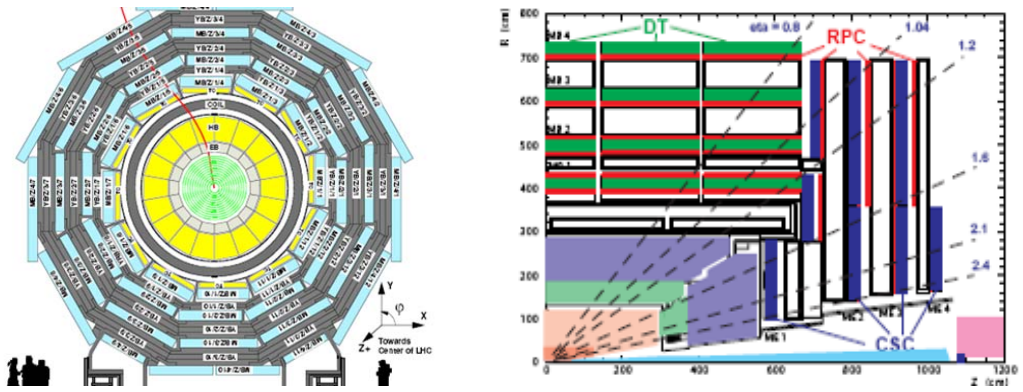


Figure 3.5: Muon chambers at CMS detector [32].

sponse. There are 1400 muon chambers: 250 DTs, 540 CSCs and 610 RPCs. The usage of a redundant system of DTs, RPCs and CSCs gives good position resolution and accurate muon identification. Particularly the DT and CSC detectors are used to obtain a precise measurement of the position and bending angle of the muons. Given that, the transverse momentum and track of the particle can be reconstructed offline. The RPC detectors are triggers which determine approximately the muon's transverse momentum.

Muons are measured three times: in the inner tracker, after the coil and in the return flux. Unlike most particles they can not be detected by calorimeters. Muons are measured by fitting a curve to hits among the four muon stations. The detector precisely can trace the particle's path, by tracking its position through the multiple layers of each station in combination with tracker measurement.

3.2.7 The trigger system

The amount of data from each bunch crossing is approximately 1MB, which at the 40MHz crossing rate would result in 40TB data each second. Most of the time, these collisions will be low- p_T and low-multiplicity processes. Therefore to reduce this huge amount of data a trigger system is designed to select the most interesting events for further analysis. Triggering of the events is done in two steps: Level-1 (L1) trigger and High Level Trigger (HLT). The L1 trigger has been designed to reduce the event rate to a maximum of 50 kHz. This data will be forward to the HLT trigger, which must reduce it further to the rate of 100 Hz.

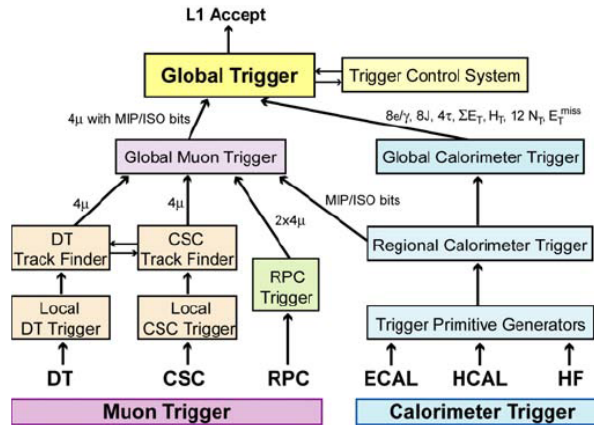


Figure 3.6: Architecture of the L1 trigger [32].

The L1 trigger architecture is depicted in Figure 3.6 which shows that it uses information from calorimeter and muon systems. No track triggers are employed at this step. Initially, all data is stored in pipelines for $3.2 \mu\text{s}$ while L1 trigger is processing. Information pass through several layers: local (calorimeter towers, muon chambers), regional (combination of towers and chambers) and global layers. Information from the Global Muon and Calorimeter Trigger is passed to the Global Trigger which decide whether to continue processing the event or to reject it. The time necessary for HLT to make a decision is 40 ms and this time more sophisticated methods are used for the selection of the events. Events that pass the HLT are saved on tape for offline analysis.

3.2.8 Data acquisition system

The CMS Data Acquisition System (DAQ) collects and analyzes electronic signals from the CMS detector after passing the L1 trigger. The CMS DAQ then will read out this data and pass it to the HLT trigger.

3.2.9 CMS computing model

The LHC will produce a huge amount of data each year therefore it presents challenges not only in terms of the physics to discover but also in terms of data volume and the necessary computing resources. Therefore the majority of the storage and processing capacity has been

distributed around the world using tiered architecture. This whole infrastructure is maintained by Worldwide LHC Computing Grid (WLCG) which has been created in service to the LHC experiments.

Tier-0 (T0)

The T0 is located at CERN and its main function is accepting and saving the RAW data (different data types explained below) from the detector after CMS DAQ and Trigger Systems. T0 do not provide analysis resources. CERN Analysis Facility (CAF) is placed also at CERN and will be used for processing the data only for very fast physics analysis. Then the data will be exported from Tier-0 to Tier-1 centers around the world.

Tier-1 (T1)

The T1 are located at large centers worldwide in CMS collaborating countries (national labs like FNAL and RAL). They will store a permanent copy of fraction of RAW data from the detector and this data will be kept at least at a minimum of two independent sites. Each T1 holds a fraction of the CMS simulated and RECO data, and complete copy of AOD data. T1 sites subsequently will provide and receive data from Tier-2 sites.

Tier-2 (T2)

There are 36 T2 centers where the final analysis of the data will be performed. T2 will produce large amount of simulated data that will be transferred back to T1 for storage. At T2 will be performed also calibration and alignment studies as well as detector analysis.

The central concept of the CMS data model is the event. The event provides access to the recorded data from a single triggered bunch crossing to new data derived from it. The event can contain raw digitized data, reconstructed products or high level analysis objects for real or simulated crossings. The event contains also information describing the origin of raw data and the provenance of all derived data products. There are several event formats for different processing steps of a data sample:

- **RAW:** This event contain the entire information from the detector including the L1 and HLT trigger results.
- **RECO:** Subsequently RAW data is processed into "RECO" format by passing through

some algorithm steps. This event contains high level physics objects and full record of the reconstructed hits.

- **AOD:** The Analysis Object Data (AOD) is obtained from RECO by filtering therefore it is a compact analysis format, designed to allow a wide range of physics analysis. It again contains high level physics objects with information needed to refit the kinematics.

3.2.10 CMS offline software framework

The CMS software (CMSSW) is built around an Event Data Model (EDM) framework. It is a collection of software needed to perform different event processing, selection and analysis tasks both to be used offline and online. It has also modular structure to be easily maintained by a large group of collaborators. Modules in the EDM framework can read the information from the event, perform some operations and then put new data into the event. There are several module types:

- Producers which add new data products into the event;
- Filters used in online triggering and selection;
- Analyzers which produce summary information from an event collection;
- Input/Output for disk storage and DAQ.

Modules are independent from the computing environment and can be executed independently. They communicate only through the event. In that meaning the EDM framework configures the modules, schedules their execution and provides access to global services. This procedure is illustrated in Figure 3.7.

3.3 Particle detection and measurement in CMS detector [33]

In general, the distance d that a particle can travel in the detector is given by

$$d = \beta c \tau = (300 \mu\text{m}) \left(\frac{\tau}{10^{-12} \text{s}} \right) \gamma \quad (3.3)$$

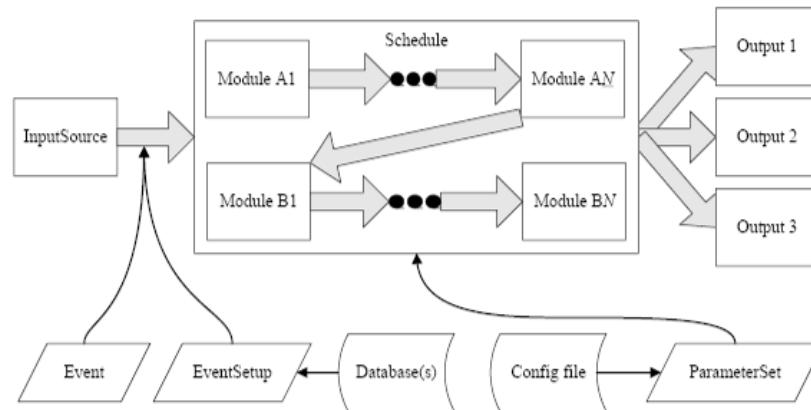


Figure 3.7: Modules within the CMS Framework [32].

where τ is the particle's proper lifetime and $\gamma = E/m$ is the relativistic factor. Equation 3.3 shows how the particles can be seen in the detector. According to their lifetime τ , they can be separated in several groups:

- Short-lived particles: Particles, like π^0 , ρ and very massive particles like Z , W^\pm , H will decay instantaneously into other particles. They can be detected only via their decay products or their reconstructed resonances.
- Particles with displaced vertex: Particles, such as $B^{0,\pm}$, $D^{0,\pm}$, τ^\pm with a lifetime $\tau \sim 10^{-12}$ s may travel some distance $\sim 100 \mu\text{m}$ before decaying and thus having a secondary vertex.
- Quasi-stable particles: These are neutral hadrons as n , Λ , K_L^0 and charged particles as μ^\pm , π^\pm , K^\pm . Their life time is $\tau > 10^{-10}$ s.
- Particles that do not interact: These particles can not be detected by the detector and lead to missing transverse energy.

All these particles can be detected in the different layers of the CMS detector based on their interactions with the materials.

Tracker

CMS tracker can record the paths of the charged particles and their electromagnetic energy loss dE/dx .

Knowing the trajectory of the particle, one can determine its momentum. Particle's momentum p can be found by using the curvature ρ of its trajectory with the following relation

$$p \propto \rho QB \quad (3.4)$$

where Q is the particle's electric charge and $B = 3.8$ T is the magnetic field. The more curved is its path, the less momentum the particle has.

The energy loss measurement dE/dx for charged particles is given by

$$\frac{dE}{dx} \propto \left(\frac{Q}{\beta}\right)^2 \quad (3.5)$$

where Q is the charge of the particle and β is its relativistic velocity. Knowing the momentum p from Equation 3.4 and the velocity β from Equation 3.5, one can identify the unknown particle by finding its mass.

ECAL

ECAL calorimeter records particle's energy by causing the particle to produce an electromagnetic shower and then measure its deposited energy. The electromagnetic shower (cascade) is due two processes: bremsstrahlung and pair production. When a particle enters ECAL, it starts showering and the number of newly created particles increase exponentially with the depth of the medium. This continue until the remaining particles has lower energy or until they are completely absorbed by the medium.

An electromagnetic shower begins when a high-energy electron or photon enters a material. The photons interact with matter via pair production. The mean free path λ for pair production by high energy photons is

$$\lambda = \frac{9}{7} X_0 \quad (3.6)$$

where X_0 is the radiation length that describes the energy decay of a beam of electrons and is given by

$$X_0 = \frac{716.4 \cdot A}{Z(Z + 1) \ln(287/\sqrt{Z})} g \cdot cm^{-2} \quad (3.7)$$

where Z is the atomic number and A is the mass number of the material.

These high energy electrons and positrons, produced by pair production, now can emit photons via bremsstrahlung. The energy loss $\frac{dE}{dx}$ of these particles by bremsstrahlung is

$$-\frac{dE}{dx} = \frac{E}{X_0}. \quad (3.8)$$

The produced photons, in turn, can lose energy by three different mechanisms:

1. Photo electric effect: absorption of a photon by an atom ejecting an electron;
2. Compton scattering;
3. Pair production.

The two processes, pair production and bremsstrahlung, continue in turn, until the remaining particles are completely absorbed by the medium.

HCAL

HCAL calorimeter records particle's energy by causing the particle to produce a hadronic shower. A hadronic shower is produced when a hadron interacts with nucleus which gives several hadrons in the final state. They subsequently interact with other nucleus to produce more hadrons. The nuclear interaction length, λ_n , for each hadron is given by the relation

$$\lambda_n \approx 35 gcm^{-2} A^{1/3} \quad (3.9)$$

where A is the mass number of the material. This process continues until all the particles are stopped or absorbed in the medium.

For heavy materials the nuclear interaction length λ_n is longer than the electromagnetic one X_0 , $\lambda_n > X_0$. This results in a later start of the hadronic showers in comparison with the electromagnetic showers. The hadronic showers are also more diffuse in comparison with electromagnetic showers.

Muon chambers

Muons are detected in the CMS muon chambers. Because of their long lifetime, they are almost like stable particles. They do not feel the strong interaction and do not initiate hadron showers in the HCAL. Therefore muons are very penetrating. At high energies, however, they can sometimes behave more like electrons. This means that the radiative losses begin to dominate and muons can bremsstrahlung, which can cause late electromagnetic showers in the detector.

Table 3.2 gives a summary of this section and shows how the different particles are detected in the CMS detector.

Table 3.2: Particle detection in different CMS layers.

Particle	Detection method
Photon	No signal in tracker; signal in ECAL; no signal in HCAL or muon chambers
Electron/positron	Signal in tracker; signal in ECAL; no signal in HCAL or muon chambers
Charged hadron (e.g. p^+ , π^- , K^+)	Signal in tracker; essentially no signal in ECAL; signal in HCAL; no signal in muon chambers
Neutral hadrons (e.g. n ...)	No signal in tracker; no signal in ECAL; signal in HCAL; no signal in muon chambers
Muon	Signal in tracker; no signal in ECAL or HCAL; signal in muon chambers
Neutrinos, SUSY particles	No signal in any sub-detector; presence inferred from missing energy

CHAPTER 4

SCALAR AND TENSOR UNPARTICLE PRODUCTION IN DIPHOTON FINAL STATE

4.1 The Photon [34]

The search for unparticles in this thesis involve photons in the final state. Below is a short description of this particle.

A photon is a quantum of the electromagnetic field that mediates the electromagnetic force between charged objects. Since electromagnetic field has Abelian U(1) gauge symmetry, the quanta of this field must be massless, have integer spin, no charge and has no self-couplings. The spin of photons is ± 1 and their right-handed and left-handed helicity, corresponding to two possible circular polarization states of photons is $\pm \hbar$.

In the SM, the photon is one of four gauge bosons in the electroweak interaction. The other three gauge bosons are W^+ , W^- and Z^0 , which unlike photon have mass. The unification of the photon with W and Z , i.e. the unification of electromagnetic and weak theory was done by S.Glashow, A.Salam and S.Weinberg, resulting in a Nobel Prize in 1979 [2].

According to quantum chromodynamics, the photon can interact both as a point-like particle, or as a collection of quarks and gluons, i.e., like a hadron. The structure of the photon is determined by its fluctuations into quark-antiquark or fermion-antifermion pairs [34]. In this case QED and QCD structure functions of the photon can be defined.

There are two types of photons. The first type is called *direct* or *bare* photon and it is regarded as a structureless object - photon as a whole takes part in the hard interaction and does not reveal its structure. The second type is called *resolved* photon. In this case, due to Heisenberg

uncertainty principle ($\Delta E \Delta t > \frac{\hbar}{2}$), the photon is allowed to violate this rule by an amount of energy ΔE for a short period of time Δt and to fluctuate into a charged fermion anti-fermion, $f\bar{f}$, system $\gamma \rightarrow f\bar{f} \rightarrow \gamma$. During such a fluctuation, one of the fermions can interact with another object and in this way to reveal the structure of the photon. In these interactions, the photon is regarded as an extended object consisting of charged fermions and gluons, therefore called *resolved* photon [35]. Various studies have been performed at LEP and HERA to study the photon structure. In our analysis, however, we are not interested in the substructures of the photon and will consider it as a whole object.

4.2 Event generation, detector simulation and reconstruction

Particle interactions in proton-proton collisions were simulated with Pythia8 [36] Monte Carlo Generator. The hard scattering process was generated using leading order matrix element calculation, followed by a parton shower evolution of the resulting partons and fragmentation forming the final state particles.

Further the generated events were processed through detector simulation and reconstruction software CMSSW to approximate the realistic experiment. The CMS detector was simulated using Fast Simulation tuned to reproduce results of the Full Simulation that uses GEANT4 software [37]. Reconstruction was done using calibration and alignment constants based on ideal conditions which means perfect calibration. No pile-up effects were considered.

4.2.1 Monte Carlo event generation

The Monte Carlo (MC) Method is commonly used in particle physics for simulation of particle collisions, interactions and decays. There are different MC generators like Pythia, Alpgen, Sherpa and Herwig that provide simulation of various particle collisions. For the generation of the unparticle signal events, we use Pythia8 MC generator. This is a program that uses theory and models for different physics processes, including hard and soft interactions, parton distributions, initial and final state parton showers, multiple interactions, fragmentation and decay. The following steps describe the generation of a typical high-energy event with Pythia8:

Hard scattering process

In proton-proton collisions only single partons take part in the hard interaction. Since partons are randomly placed inside the hadron, their distribution must be taken into account. This is realized using Parton Distribution Functions (PDFs), $f_i(x, Q^2)$. PDFs describe the probability to find a parton i inside a proton, with parton i carrying a fraction x of the total proton's momentum. PDFs depend on some scale Q^2 that characterizes the hard process and they are obtained from global fits to deep inelastic scattering and other data. The most widely used sets PDFs are provided by CTEQ [38] and MRST [39] groups and HERA collaboration.

To find the differential cross section of the hard process, we use the QCD factorization theorem which states that the hadronic cross section σ_{AB} is a convolution of the partonic cross section $\hat{\sigma}^{ij}$ with PDFs $f_{i,j}(x, Q^2)$. Additionally, all possible combinations of incoming partons are summed to find the total cross section of the hard process given by the relation

$$\sigma_{AB}(s, Q^2) = \sum_{i,j} \int dx_i dx_j f_i(x, Q^2) f_j(x, Q^2) d\hat{\sigma}^{ij}(x_i, x_j, Q^2) \quad (4.1)$$

where s is center of mass energy and A/B denotes the incoming hadrons.

Pythia consider only three level diagrams and is restricted to maximum two particles in the final state. However other generators may have more than two particles in the final state.

The outgoing particles from the hard process may further decay. Therefore they enter the process of fragmentation and hadronization.

Parton shower and fragmentation

The hard process is calculated to lowest order (LO) of perturbation theory. However it depends strongly on the renormalization (Q_R) and factorization scales (Q_F). Often LO calculations are not sufficient to fit the experimental data and next to leading order (NLO) or higher order calculations are necessary. Higher order calculations add an extra factor α_s to the original Feynman diagram which means further quarks and gluons are included in the process. The initial and final parton shower approach implemented in Pythia accounts for these higher order QCD effects.

The shower evolution of partons down to lower energies is followed by their confinement

into hadrons via string fragmentation (hadronization) according to some phenomenological models. The hadronization is based solely on the Lund string fragmentation framework [40].

Figure 4.1 illustrates the complex variety of processes taking place in a single proton-proton collision. Beside hard scattering, showering and fragmentation, the partons of the incoming hadrons can undergo soft interactions as well. These are the partons that do not participate in the hard process and their interactions are modeled by minimum bias collisions (underlying event).

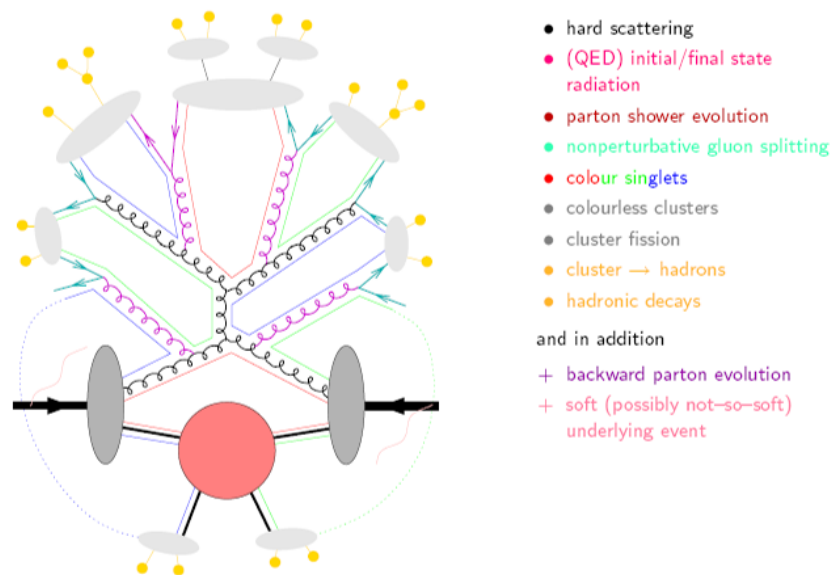


Figure 4.1: Pythia processes.

4.2.2 Detector simulation and reconstruction

To simulate the CMS detector, we use Fast Simulation program. This is a C++ program which simulates the particle interaction with matter. Basically, the generated events with Pythia8 are propagated through the magnetic field and a simulation of their interaction with the different detector components is performed. This data is stored in the form of hits which contain information about particle's position and momentum, or the energy deposited in the detector. Fast Simulation does not use the detailed simulation of the CMS detector but instead a more simplified structure. There is a Full Detector Simulation which is based on GEANT4 and it is about 1000 times slower than Fast Simulation. However it has been shown that the results

with the Fast Simulation are in a good agreement with the results based on Full Detector Simulation.

After the simulation procedure, the hits are reconstructed. The reconstruction is done again with the same Fast Simulation program into physics objects like muons, electrons, photons, jets and missing transverse energy. Depending on the type of the detector, particles are reconstructed using different algorithms.

In this analysis we have two photons in the final state. In general, photons are detected in ECAL, as this is the subdetector where they deposit their energy. There are also other requirements in order one object to be identified in the detector as a photon. In what follows, it is explained in detail how photons are detected, reconstructed and identified in CMS.

Photon identification in CMS

Photons are reconstructed by considering electromagnetic superclusters in the ECAL. These superclusters are clusters of basic clusters, consisting of 5×5 cells. The clustering algorithm is described in detail in [41]. A supercluster that passes loose requirements on the ratio of the ECAL and HCAL energies is considered a photon candidate. However both electrons and photons can be reconstructed as photon candidates. Therefore one can scan the pixel detector for the presence of hits. Electrons as charged particles leave trace in the pixel detector of the tracker, in comparison with photons that do not leave any trace there. If matching pixel hits consistent with the trajectory of the particle are found, this photon candidate is not used in the analysis.

The main instrumental background to photons originates from jets fragmenting in π^0 or η mesons, decaying subsequently into a pair of close photons. This background can be reduced by using the following requirements on a set of isolation variables which gives the Photon ID (requirements to claim that one object is a photon):

- **H/E** compares the sum of the E_T of hits in the HCAL in a cone of radius $\Delta R < 0.05$ behind the supercluster found in the ECAL to the E_T of that supercluster.
- **ECAL Isolation** considers the sum of the E_T of ECAL RecHits within a hollow cone of $0.06 < \Delta R < 0.40$ around a supercluster in the ECAL, excluding clusters which belong to that cluster. It is required that the ECAL isolation is < 10 GeV.

- **HCAL Isolation** considers the sum of the E_T of HCAL RecHits within a hollow cone of $0.10 < \Delta R < 0.40$ about the supercluster. It is required that < 5.0 GeV.
- **Tracking number isolation** considers the sum of the p_T of tracks found in the silicon tracker less than 5 GeV within in a hollow cone of $0.04 < \Delta R < 0.40$ around the supercluster found in the ECAL.

where ΔR is defined as

$$\Delta R = \sqrt{(\Delta\eta)^2 + (\Delta\phi)^2} \quad (4.2)$$

in (η, ϕ) space.

4.3 Unparticle signal

4.3.1 Signal generation with Pythia8

Unparticles can be produced through different channels as discussed in Chapter 2. For this analysis, we are interested in virtual unparticle production that subsequently decay to two photons.

In general, two photons γ with momenta p_i , can be produced in hadron collider through

$$P_1(p_1) + P_2(p_2) \rightarrow \gamma(p_3) + \gamma(p_4) + X(p_X), \quad (4.3)$$

where P_i are the incoming hadrons with momenta p_i and X is the final inclusive hadronic state. The hadronic cross section can be obtained from partonic cross sections $d\hat{\sigma}^{ab}$ by using appropriate PDF

$$d\sigma(P_1 P_2 \rightarrow \gamma\gamma X) = \sum_{a,b=q,\bar{q},g} \int f_a^{P_1}(x_1) f_b^{P_2}(x_2) d\hat{\sigma}^{ab}(x_1, x_2) dx_1 dx_2 \quad (4.4)$$

where x_1 and x_2 are the momentum fractions of the incoming partons in the hadrons P_1 and P_2 .

In this analysis, which is based to LO in QCD, we are interested only in spin-0 and spin-2 unparticle production in diphoton final state. Below are the squared matrix elements [42] for $q\bar{q}$ annihilation and gg fusion with scalar and tensor unparticles appearing as propagators which leads to two photons in the final state.

Spin-0:

$$\begin{aligned} |\bar{M}_{q\bar{q}}|^2 &= \frac{1}{8N_c} \lambda_s^4 \chi^2 u \left(\frac{s}{\Lambda_u^2} \right)^{2d_u-1} \\ |\bar{M}_{gg}^2 &= \frac{1}{8(N_c^2 - 1)} \frac{1}{4} \lambda_s^4 \chi^2 u \left(\frac{s}{\Lambda_u^2} \right)^{2d_u} \end{aligned} \quad (4.5)$$

Spin-2:

$$\begin{aligned} |\bar{M}_{q\bar{q}}|^2 &= \frac{1}{8N_c} \left[e^4 Q_f^4 8 \left(\frac{u}{t} + \frac{t}{u} \right) \right. \\ &\quad - 8e^2 Q_f^2 \lambda_t^2 \chi u \cos(d_u \pi) \left(\frac{s}{\Lambda_u^2} \right)^{d_u} \frac{1}{s^2} (u^2 + t^2) \\ &\quad \left. + 2\lambda_t^4 \chi^2 u \left(\frac{s}{\Lambda_u^2} \right)^{2d_u} \frac{1}{s^4} (u^2 + t^2) \right], \\ |\bar{M}_{gg}^2 &= \frac{1}{8(N_c^2 - 1)} 2\lambda_t^4 \chi^2 u \left(\frac{s}{\Lambda_u^2} \right)^{2d_u} \frac{1}{s^4} (u^2 + t^2). \end{aligned} \quad (4.6)$$

with

$$\chi u = \frac{A_{d_u}}{(2 \sin(d_u \pi))} \quad A_{d_u} = \frac{16\pi^{5/2}}{(2\pi)^{2d_u}} \frac{\Gamma(d_u + 1/2)}{\Gamma(d_u - 1)\Gamma(2d_u)} \quad (4.7)$$

where Q_f is electric charge of the parton flavor f , N_c is the number of colors and s , t and u are Mandelstam invariants.

In order this process to occur, it is required that scaling dimension d_u takes values, $1 < d_u < 2$. The lower bound corresponds to the least stringent unitarity constraint, obtained for scalar unparticles. For $d_u > 2$, contributions that depends on the UV completion of the theory are relevant, which suggests that the effective theory used will not be valid. In this analysis we

assume the same range of values for $d_{\mathcal{U}}$, valid for tensor unparticles as well.¹ The couplings of the unparticles to SM fields are given by

$$\lambda_k = C_{\mathcal{U}}^k \left(\frac{\Lambda_{\mathcal{U}}}{M_{\mathcal{U}}} \right)^{d_{\mathcal{B}Z}} \frac{1}{M_{\mathcal{U}}^{d_{SM}-4}} \quad (4.8)$$

where k stands for scalar (s) or tensor (t) coupling. We assume that $0.4 < \lambda_k < 1$, in order to work in perturbation regime.

The signal for spin-0 and spin-2 unparticle for different unparticle model parameters has been generated using the Pythia8 event generator:

1. Scale dimension parameter - $d_{\mathcal{U}}$;
2. Unparticle renormalization scale - $\Lambda_{\mathcal{U}} = 1 \text{ TeV}$;
3. Coupling constant - λ .

Scalar unparticles do not interfere with SM diphoton production processes and hence the individual cross sections of the unparticle contribution to the total diphoton production cross section are calculated. Tensor unparticles do interfere with SM production and hence for the spin-2 case, the matrix elements include full interference with the corresponding tree level processes in the SM.

Spin-0 and spin-2 unparticle samples for various unparticle parameters were generated with minimum cut on the invariant mass of two photons of 100 GeV. Their production cross sections are listed in Table 4.1. The SM cross section, with the same minimum diphoton mass cut of 100 GeV, was found to be 25.45 pb. The generation of these events was done in center of mass energy $\sqrt{s} = 10 \text{ TeV}$.

Figure 4.2 shows an example of single Pythia event and the integrated cross sections for spin-0 unparticle generation with $\lambda = 0.9$, $d_{\mathcal{U}} = 1.01$ and $\Lambda_{\mathcal{U}} = 1 \text{ TeV}$. All the particles that emerge after the collision of two protons are listed. In general, we are interested only in the hard process which means only calculation of the LO cross section of scalar and tensor unparticle

¹ Recent analysis constrains the value of scaling dimension, $d_{\mathcal{U}} > 4$ [43], for tensor unparticles. For the completeness of this work, we assume that the same range of values of $d_{\mathcal{U}}$ for scalar unparticle are valid for tensor unparticle as well.

Table 4.1: LO scalar and tensor unparticle cross sections for $\Lambda_{\mathcal{U}} = 1$ TeV as a function of the scale dimension parameter and the coupling constant.

$d_{\mathcal{U}}$	λ	$\sigma(\text{Signal+SM}), \text{pb}$ Scalar unparticles	$\sigma(\text{Signal+SM}), \text{pb}$ Tensor unparticles
1.01	0.9	29.25	25.54
1.1	0.9	26.56	25.43
1.2	0.9	25.80	25.41
1.3	0.9	25.58	25.47
1.5	0.9	25.49	25.47
1.7	0.9	25.46	25.45
1.9	0.9	25.47	25.46
1.01	0.2	25.48	25.44
1.01	0.4	25.64	25.35
1.01	0.6	26.19	25.32
1.01	0.8	27.86	25.41
1.01	1.0	31.23	25.78

that can lead to two photons. The NLO cross section of unparticle production also has been considered later in this analysis by using a K-factor of 1.3.

4.3.2 Kinematical distributions

In this section we show some kinematical distributions (see Appendix A for definition of kinematical variables) of the diphotons mediated by virtual unparticle exchange. The generation of the events was done as explained in Section 4.3.1.

To unravel the unparticle signature, all unparticle distributions of two photons are compared with the SM diphoton production. For all distributions is used MRST 2001 LO PDF [44] and the following cuts, found to be optimal [42] for this analysis:

1. $p_T^\gamma > 40$ GeV;
2. $|y^\gamma| < 2.5$;

where p_T^γ and y^γ are transverse momentum and rapidity of the photons. These cuts were applied in order to be as close as possible to the experimental setup. To suppress the SM background, some additional cuts were also applied to particular distributions in the following way:

PYTHIA Event Listing (hard process)											Pythia Event				
no	id	name	status	mothers	daughters	colours	p_x	p_y	p_z	e	m				
0	90	(system)	-11	0	0	0	0.000	0.000	0.000	10000.000	10000.000				
1	2212	(p+)	-12	0	3	0	0.000	0.000	5000.000	5000.000	0.938				
2	2212	(p+)	-12	0	0	0	0.000	0.000	-5000.000	5000.000	0.938				
3	-2	(ubar)	-21	0	5	6	101	0.000	0.000	3.319	3.319				
4	-2	(u)	-21	2	0	0	0.000	0.000	-1243.627	1243.627	0.000				
5	22	gamma	23	3	4	0	0	4.084	2.867	-1241.743	1241.753	0.000			
6	22	gamma	23	3	4	0	0	-4.084	-2.867	1.435	5.193	0.000			
Charge sum: 0.000							Momentum sum: 0.000 0.000 -1240.308 1246.945 128.487								
End PYTHIA Event Listing															
PYTHIA Event Listing (complete event)															
no	id	name	status	mothers	daughters	colours	p_x	p_y	p_z	e	m				
0	90	(system)	-11	0	0	0	0.000	0.000	0.000	10000.000	10000.000				
1	2212	(p+)	-12	0	7	0	0.000	0.000	5000.000	5000.000	0.938				
2	2212	(p+)	-12	0	0	0	0.000	0.000	-5000.000	5000.000	0.938				
3	-2	(ubar)	-21	7	5	6	101	0.000	0.000	3.319	3.319				
4	-2	(u)	-21	8	8	5	6	101	0.000	0.000	-1243.627	1243.627			
5	22	(gamma)	-23	3	4	0	0	4.084	2.867	-1241.743	1241.753				
6	22	(gamma)	-23	3	4	10	10	0	-4.084	-2.867	1.435	5.193			
7	-2	(ubar)	-61	1	0	3	0	101	1.167	-0.253	2.711	4.436			
8	-2	(u)	-61	2	0	4	4	101	0.475	-1.080	-1243.563	1243.563			
9	22	gamma	62	5	5	0	0	0	2.920	-3.119	1.936	4.691			
10	22	gamma	62	5	5	0	0	0	3.611	3.946	-1242.287	1242.299			
11	2	(u)	-63	1	0	21	21	101	0	-0.417	0.864	1242.563	1242.563		
12	2101	(ud_0)	-63	1	0	16	16	0	-0.606	-0.320	3735.752	3735.753			
13	2	(u)	-63	1	0	15	15	103	0	-0.144	-0.291	18.363	18.368		
14	2101	(ud_0)	-63	2	0	22	22	0	0.475	-1.080	-3756.326	3756.326			
15	2	(u)	-71	12	13	17	20	103	0	-0.144	-0.291	18.363	18.368		
16	2101	(ud_0)	-71	12	12	17	20	0	-0.606	-0.320	3735.752	3735.753			
17	113	(rho0)	-83	15	16	37	38	0	-0.004	-0.068	94.337	94.341			
18	211	(rho+)	-83	15	16	0	0	0	0.399	-0.102	80.651	80.652			
19	1114	(delta-)	-84	15	16	39	40	0	-1.103	-0.054	2041.151	2041.152			
20	213	(rho+)	-84	15	16	41	42	0	-0.042	-0.387	1537.975	1537.976			
21	2	(u)	-71	11	11	23	36	101	0	-0.417	0.864	1242.563	1242.563		
22	2101	(ud_0)	-71	14	14	23	36	0	0.475	-1.080	-3756.326	3756.326			
23	213	(rho+)	-83	21	22	43	44	0	0	0.257	0.571	268.565	268.567		
24	223	(omega)	-83	21	22	55	57	0	-0.257	-0.186	337.629	337.630			
25	-211	(pi-)	-83	21	22	0	0	0	-0.093	0.941	33.723	33.723			
26	223	(omega)	-83	21	22	58	60	0	-0.088	-0.734	394.588	394.590			
27	223	(omega)	-83	21	22	61	63	0	0.392	-0.186	198.582	198.584			
28	113	(rho0)	-83	21	22	45	46	0	0.250	-0.178	4.908	4.908			
29	321	(k+)	-83	21	22	0	0	0	-0.477	0.101	4.345	4.400			
30	-313	(k*bar0)	-83	21	22	47	48	0	-0.054	0.100	-1.486	1.717			
31	-211	(pi-)	-83	21	22	0	0	0	-0.023	-0.140	-0.616	0.648			
32	323	(k*+)	-84	21	22	49	50	0	0.122	-0.012	-31.018	31.031			
33	-313	(k*bar0)	-84	21	22	51	52	0	-0.124	0.221	-31.673	31.693			
34	-211	(pi-)	-84	21	22	0	0	0	-0.295	-0.368	-52.572	52.574			
35	211	(pi+)	84	21	22	0	0	0	0.009	-0.466	-120.736	120.737			
36	2112	(pi0)	84	21	22	0	0	0	0.776	-0.448	-3518.002	3518.002			
37	211	(pi+)	91	17	0	0	0	0	-0.049	-0.394	31.187	31.190			
38	211	(pi+)	91	17	0	0	0	0	0.045	-0.326	63.150	63.151			
39	2112	(pi0)	91	19	0	0	0	0	-0.541	-0.023	1391.837	1391.838			
40	-211	(pi-)	91	19	0	0	0	0	-0.562	-0.031	649.314	649.314			
41	211	(pi+)	91	20	0	0	0	0	0.208	-0.146	1187.493	1187.493			
42	111	(pi0)	-91	20	0	64	65	0	-0.250	-0.241	350.483	350.483			
43	211	(pi+)	91	20	0	0	0	0	0.082	0.463	91.657	91.659			
44	111	(pi0)	-91	23	0	66	67	0	-0.324	-0.106	176.908	176.908			
45	211	(pi+)	91	28	0	0	0	0	0.400	0.039	4.196	4.218			
46	-211	(pi-)	91	28	0	0	0	0	-0.170	-0.217	0.712	0.776			
47	-321	(k-)	91	30	0	0	0	0	-0.008	-0.191	-0.839	0.992			
48	211	(pi+)	91	30	0	0	0	0	-0.047	0.291	-0.648	0.725			
49	311	(rho0)	-91	32	16	53	53	0	0.392	0.079	29.184	29.188			
50	211	(pi+)	91	32	0	0	0	0	0.050	-0.091	-1.835	1.843			
51	-311	(k*bar0)	-91	33	0	54	54	0	-0.491	0.250	-19.969	19.983			
52	111	(pi0)	-91	33	0	68	70	0	0.358	-0.028	-11.704	11.710			
53	130	(k_L0)	91	49	49	0	0	0	0.072	0.079	-29.184	29.188			
54	130	(k_L0)	91	51	51	0	0	0	-0.491	0.250	-19.969	19.983			
55	211	(pi+)	91	24	0	0	0	0	-0.338	-0.219	209.821	209.822			
56	-211	(pi-)	91	24	0	0	0	0	0.020	0.132	89.278	89.278			
57	111	(pi0)	-91	24	0	71	72	0	0.062	-0.099	38.530	38.530			
58	211	(pi+)	91	26	0	0	0	0	-0.236	0.319	102.840	102.840			
59	-211	(pi-)	91	26	0	0	0	0	0.000	0.289	216.245	216.245			
60	111	(pi0)	-91	26	0	73	74	0	0.148	0.126	75.504	75.504			
61	211	(pi+)	91	27	0	0	0	0	0.038	-0.214	35.803	35.804			
62	-211	(pi-)	91	27	0	0	0	0	0.412	-0.122	88.588	88.589			
63	111	(pi0)	-91	27	0	75	76	0	0.143	0.150	74.191	74.191			
64	22	gamma	91	42	0	0	0	0	-0.130	-0.087	215.499	215.499			
65	22	gamma	91	42	0	0	0	0	-0.120	-0.154	134.983	134.984			
66	22	gamma	91	44	0	0	0	0	-0.098	0.094	76.221	76.221			
67	22	gamma	91	44	0	0	0	0	-0.236	0.013	100.687	100.687			
68	22	gamma	91	52	0	0	0	0	0.277	-0.008	-6.921	6.927			
69	11	(e+)	91	52	0	0	0	0	0.078	-0.020	-4.656	4.656			
70	-11	(e-)	91	52	0	0	0	0	0.003	-0.001	-0.127	0.127			
71	22	gamma	91	57	0	0	0	0	-0.005	-0.009	23.183	23.183			
72	22	gamma	91	57	0	0	0	0	0.067	-0.090	15.346	15.347			
73	22	gamma	91	60	0	0	0	0	0.024	-0.029	9.675	9.675			
74	22	gamma	91	60	0	0	0	0	0.124	0.154	65.828	65.829			
75	22	gamma	91	63	0	0	0	0	0.007	0.023	1.657	1.657			
76	22	gamma	91	63	0	0	0	0	0.136	0.127	72.534	72.535			
Charge sum: 2.000							Momentum sum: -0.000 -0.000 0.000 10000.000 10000.000								
End PYTHIA Event Listing															
PYTHIA Event and Cross Section Statistics															
Subprocess	Code	Number of events			sigma +- delta (estimated) (mb)										
		Tried	Selected	Accepted											
f fbar -> gamma gamma	204	7763417	871371	871371	2.549e-08	1.347e-11									
f fbar -> (u*) -> gamma gamma	5043	561689	121300	121300	3.546e-09	5.860e-12									
g g -> (u*) -> gamma gamma	5044	58031	7329	7329	2.153e-10	1.566e-12									
sum		8383137	1000000	1000000	2.925e-08	1.477e-11									
End PYTHIA Event and Cross Section Statistics															

Figure 4.2: Single Pythia event listing and integrated cross sections for spin-0 unparticle with $\lambda_s = 0.9$, $d_{\mathcal{U}} = 1.01$ and $\Lambda_{\mathcal{U}} = 1$ TeV in diphoton final state.

- For invariant mass distribution is applied an angular cut

$$|\cos \theta_\gamma| < 0.8. \quad (4.9)$$

where θ_γ is the angle of the photons in the lab frame.

- For angular and rapidity distributions is applied cut on the invariant mass

$$600\text{GeV} < Q < 900\text{GeV}. \quad (4.10)$$

All unparticle distributions plotted here include both unparticle and SM contributions. Additionally, the SM background alone is presented in the same plots as well. The SM background includes only Born process (quark, antiquark annihilation). Box process (gluon fusion) has not been considered in this analysis since its negligible contribution.

Invariant mass distribution

Invariant mass distributions are shown in Figures 4.3 and 4.4. In Figure 4.3 is plotted the diphoton invariant mass that depends on different choices of scaling dimension d_U . Figure 4.4 illustrates the invariant mass dependence on the coupling λ_s/λ_t for scalar/tensor unparticle. The unparticle effects can be seen at large invariant mass values when decreasing the scaling dimension d_U and increasing the couplings λ_s/λ_t .

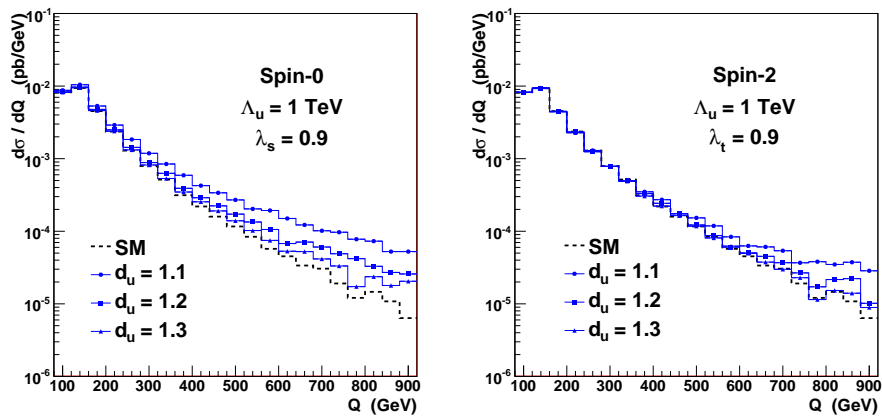


Figure 4.3: Invariant mass distribution for spin-0 (left) and spin-2 (right) unparticle, plotted for various values of dimension parameter d_U with $\Lambda_U = 1 \text{ TeV}$ and $\lambda_s, \lambda_t = 0.9$.

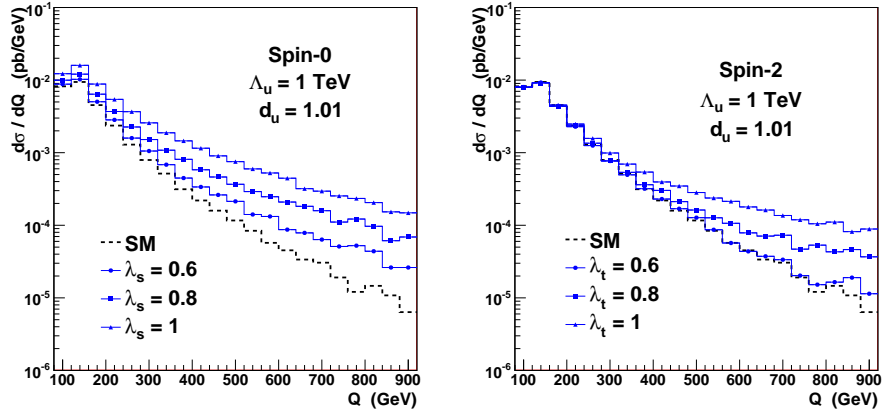


Figure 4.4: Invariant mass distribution for spin-0 (left) and spin-2 (right) unparticle with $\Lambda_u = 1$ TeV and $d_u = 1.01$, plotted for various values of the couplings λ_s and λ_t .

Angular distribution

Angular distribution $d\sigma/d\cos\theta^*$ is studied in the CM frame of the final state photons where the angle θ^* is defined by

$$\cos\theta^* = \frac{p_1 \cdot (p_3 - p_4)}{p_1 \cdot (p_3 + p_4)} \quad (4.11)$$

with final state photon momenta p_3 and p_4 . p_1 is the momentum of the incoming protons.

Angular distributions for spin-0 and spin-2 unparticle are shown in Figure 4.5. They can be easily distinguished from the SM distribution because of its specific shape. For spin-2 unparticle case, for $\lambda_t = 0.4$, there is a negative interference with the SM and this brings down the distribution.

Rapidity distribution

Rapidity distribution in Figure 4.6 of the diphoton system is defined as

$$Y = \frac{1}{2} \log\left(\frac{p_2 \cdot q}{p_1 \cdot q}\right) \quad (4.12)$$

where $q = p_3 + p_4$ is the sum of the final state photon momenta and p_1 , and p_2 are momenta of the incoming protons. Deviation from the SM can be seen which is particularly large at the

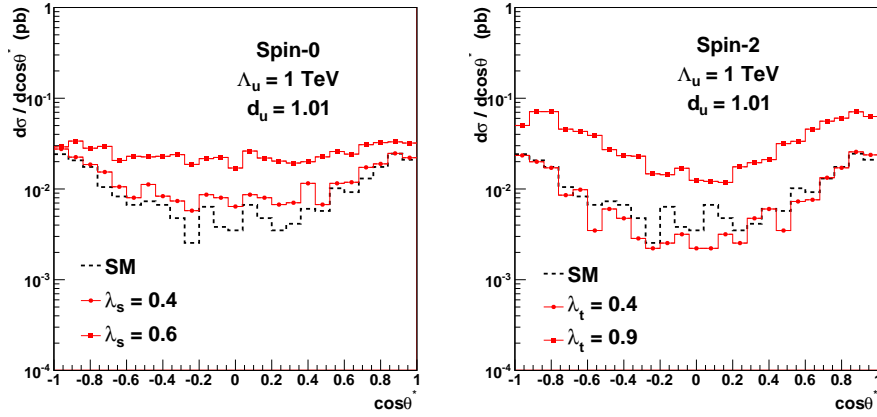


Figure 4.5: Angular distribution for spin-0 (left) and spin-2 (right) unparticle with $\Lambda_U = 1$ TeV and $d_U = 1.01$, plotted for various values of the couplings λ_s and λ_t .

central region. In general, it can be concluded that for spin-0 unparticle the unparticle effects are large whereas for spin-2 unparticle they are significant only for large values of λ_t .

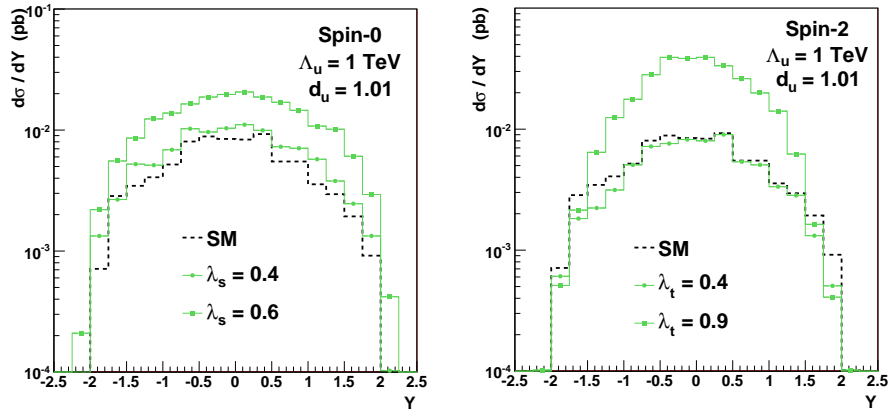


Figure 4.6: Rapidity distribution of diphoton system for spin-0 (left) and spin-2 (right) unparticle with $\Lambda_U = 1$ TeV and $d_U = 1.01$, plotted for various values of the couplings λ_s and λ_t .

From the various kinematical distribution that were studied here, it can be concluded that spin-0 and spin-2 unparticle can be clearly distinguished from the SM background, by an order of magnitude, in most of the distributions that we have considered. We conclude that for coupling values λ and scaling dimension d_U close to 1 the unparticle effects are most observable.

4.4 Background

The main backgrounds to the unparticle diphoton signal are:

- SM diphoton production from quark anti-quark annihilation (Born process);
- SM diphoton production from gluon fusion (Box process);
- Photon+Jets;
- QCD multijets;
- Drell-Yan e^+e^- .

The Born and Box diphoton backgrounds are irreducible backgrounds since their final state is exactly the same as that for the signal. The box diagram background has not been considered in this analysis since its contribution is negligible at high diphoton masses used in the analysis.

In Photon+Jet background, the gluon jet fragmentation leads to a leading π^0/η , which decays into a pair of closely spaced photons, thus leading to the diphoton signature. Similarly the multijet events can lead to a diphoton background.

The Drell-Yan background arises when the electron tracks are not reconstructed or when photons are produced via bremsstrahlung of the electrons.

The expected amount of instrumental background from Photon+Jets, QCD dijets, and Drell-Yan has been evaluated in [45], and was found to be insignificant for our analysis.

Therefore, in this analysis we assume that the main background comes from Born diphoton production. The Born background was generated with Pythia8 Monte Carlo Generator and again processed through Fast Simulation for detector simulation. For completeness, in what follows, we give short theoretical description of LO and NLO SM diphoton production processes. In this work, the NLO processes have been taken into account by multiplying the SM Born cross section by appropriate K-factor.

4.4.1 SM diphoton production [46]

4.4.1.1 LO processes

The SM two photons can be produced in several ways:

1. Born process - quark anti-quark annihilation;
2. Single photon bremsstrahlung - a single photon with the second coming from bremsstrahlung from a quark;
3. Double photon bremsstrahlung - both photons are produced by bremsstrahlung;
4. Box process - gluon fusion.

Born process

Born process is given by the following relation

$$q(p_1) + \bar{q}(p_2) \rightarrow \gamma(p_3) + \gamma(p_4) \quad (4.13)$$

with Feynman diagrams shown in Figure 4.7.

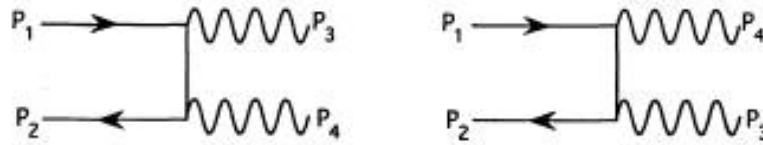


Figure 4.7: Feynman diagrams for the Born subprocess $q\bar{q} \rightarrow \gamma\gamma$. The straight and wavy lines denote quarks and photons, respectively [46].

The squared amplitude M^{Born} of this process summed over final state polarizations and initial state spins is given by

$$|M^{Born}|^2 = 8N_C\alpha^4 Q_q^4 \mu^{4\epsilon} (1 - \epsilon) \times \left[(1 - \epsilon) \left(\frac{t}{u} + \frac{u}{t} \right) - 2\epsilon \right] \quad (4.14)$$

where N_C is the number of colors, α is the electromagnetic coupling constant, Q_q is the electric charge of the quark, μ is mass parameter introduced to keep the couplings dimensionless and $N = 4 - 2\epsilon$ is the number of space-time dimensions. The kinematic invariants s , t and u are defined as

$$s = (p_1 + p_2)^2, \quad t = (p_1 - p_3)^2, \quad u = (p_1 - p_4)^2. \quad (4.15)$$

with momenta p_1 , p_2 , p_3 and p_4 as given in Figure 4.7.

The Born cross section was found to be

$$d\hat{\sigma}(q\bar{q} \rightarrow \gamma\gamma) = \frac{1}{4} \frac{1}{9} \frac{1}{2} \frac{1}{2s} |M^{Born}|^2 d^N \Phi_2 \quad (4.16)$$

where the factors $\frac{1}{4}$, $\frac{1}{9}$ and $\frac{1}{2}$ are the spin average, color average, and identical particle factors. The two body phase space $d^N \Phi_2$ is

$$d^N \Phi_2 = \frac{1}{8\pi} \left(\frac{4\pi}{s} \right)^\epsilon \frac{1}{\Gamma(1-\epsilon)} v^{-\epsilon} (1-v)^{-\epsilon} dv \quad (4.17)$$

with $v = \frac{1}{2}(1 + \cos \theta)$. The final Born cross section is obtained by convoluting the Born subprocess cross section with the parton densities and summing over the contributing partons. It takes the following form

$$\begin{aligned} \sigma^{Born}(AB \rightarrow \gamma\gamma) &= \sum_q \int d\hat{\sigma}^{Born}(q\bar{q} \rightarrow \gamma\gamma) \\ &\times \left[G_{q/A}(x_1, Q^2) G_{\bar{q}/B}(x_2, Q^2) + (x_1 \leftrightarrow x_2) \right] dx_1 dx_2 \end{aligned} \quad (4.18)$$

where $G_{q/A}(x_1)/G_{\bar{q}/B}(x_2)$ denotes the probability of finding a quark/antiquark in hadron A/B , Q is the scale at which this reaction occurs and is prescribed by perturbation theory (e.g. Altarelli - Parisi equation).

Single photon bremsstrahlung

Single photon bremsstrahlung occurs via the process

$$qg \rightarrow \gamma q \quad (4.19)$$

where the second photon is produced from the final state quark. The cross section for single photon bremsstrahlung is

$$\begin{aligned} \sigma_{1brem}(AB \rightarrow C\gamma) &= \sum_{a,b,c} \int G_{a/A}(x_a, Q^2) G_{b/B}(x_b, Q^2) \times D_{\gamma/c}(z_c, Q_f^2) \\ &\times \frac{d\hat{\sigma}}{dv}(ab \rightarrow c\gamma) dx_a dx_b dz_c dv \end{aligned} \quad (4.20)$$

where $G_{a/A}(x_a)/G_{b/B}(x_b)$ denotes the probability of finding a parton a/b in a hadron A/B with a momentum fraction lying between x_a/x_b and $x_a + dx_a/x_b + dx_b$. The probability of obtaining a hadron C with a momentum fraction between z_c and $z_c + dz_c$ is denoted by the fragmentation function $D_{\gamma/c}$. Q and Q_f are the factorization scales for the distribution and fragmentation functions.

Double photon bremsstrahlung

In the double photon bremsstrahlung process, the two photons are produced from final state quarks. The possible subprocesses with two quarks in the final state are listed below:

- $qq \rightarrow (q \rightarrow \gamma)(q \rightarrow \gamma)$
- $gq \rightarrow (g \rightarrow \gamma)(q \rightarrow \gamma)$
- $gg \rightarrow (g \rightarrow \gamma)(g \rightarrow \gamma)$

The cross section for these processes is given by the formula

$$\begin{aligned} \sigma_{2brem}(AB \rightarrow CD) &= \sum_{a,b,c,d} \int G_{a/A}(x_a, Q^2) G_{b/B}(x_b, Q^2) \times D_{\gamma/c}(z_c, Q_f^2) D_{\gamma/d}(z_d, Q_f^2) \\ &\times \frac{d\hat{\sigma}}{dv}(ab \rightarrow cd) dx_a dx_b dz_c dz_d dv. \end{aligned} \quad (4.21)$$

where $G_{a/A}(x_a)/G_{b/B}(x_b)$ denotes the probability of finding a parton a/b in a hadron A/B with a momentum fraction lying between x_a/x_b and $x_a + dx_a/x_b + dx_b$. $D_{\gamma/c}/D_{\gamma/d}$ denotes the

probability of obtaining a hadron C/D with a momentum fraction between z_c and $z_c + dz_c/z_d$ and $z_d + dz_d$.

Thus the cross section for $\gamma\gamma$ production including born process, single and double photon bremsstrahlung is

$$\sigma^* = \sigma^{Born} + \sigma_{1brem} + \sigma_{2brem}. \quad (4.22)$$

Box process: $gg \rightarrow \gamma\gamma$

Although this process is of order α_s^2 , the cross section becomes large at high CM energies due to large gluon density at small values of the parton momentum fraction x from the hadron's momentum. Figure 4.8 shows Box Feynman diagram.

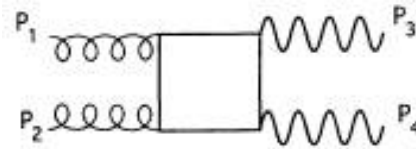


Figure 4.8: Feynman diagrams for the Box subprocess $gg \rightarrow \gamma\gamma$. The straight, wavy and curly lines denote quarks, photons and gluons, respectively [46].

The cross section of this process can be found in [47].

4.4.1.2 NLO processes

When higher order subprocesses are considered, one encounters a variety of singularities such as infrared (soft), ultraviolet and collinear singularities. All of them can be factorized or separated from the relevant processes. When some of the singularities are absorbed into distribution and fragmentation functions and others regulated by some technique (such as dimensional regularization), this is known as renormalization process. In [46] they are discussed in details and the corrections to the diphoton cross sections are given. The NLO contribution to the LO diphoton production as discussed in the same article comes from:

1. Virtual processes - their Feynman diagrams are shown in Figure 4.9.

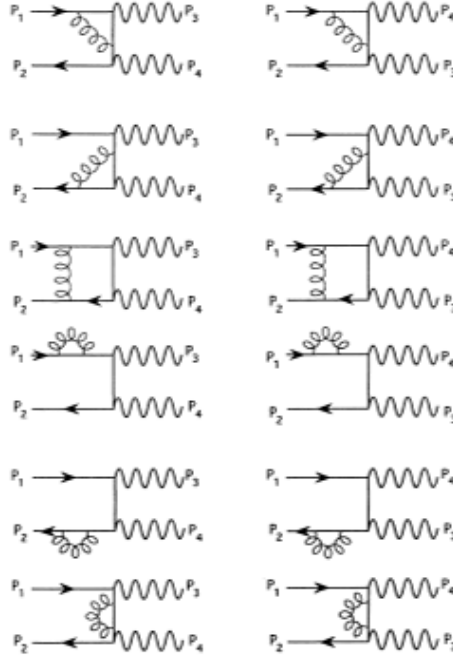


Figure 4.9: Feynman diagrams for the virtual subprocess $q\bar{q} \rightarrow \gamma\gamma$ [46].

2. Soft gluon emission - their Feynman diagrams are shown in Figure 4.10.

Singularities from virtual processes and soft gluon emission will cancel each other when the graphs from Figures 4.9 and 4.10 are added together.

3. Collinear radiation from initial state partons - when at least one photon's momentum is collinear to the momentum of initial state parton. These singularities are absorbed in the initial state PDFs. More details can be found in [46].
4. Collinear radiation from final state partons - when at least one photon's momentum is collinear to the momentum of final state parton. These singularities are absorbed in the final state fragmentation functions.

The final cross section σ after summing up all the contributions from born process, single and double bremsstrahlung and all the corrections from higher order contributions is given by

$$\sigma = \sigma^* + \sigma^{virt} + \sigma^{soft} - \sigma^{collinear}. \quad (4.23)$$

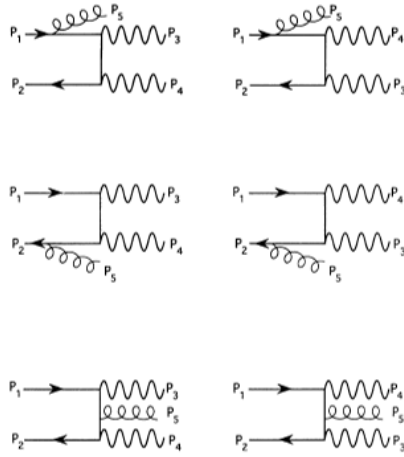


Figure 4.10: Feynman diagrams for the real emission process $q\bar{q} \rightarrow \gamma\gamma g$ [46].

4.5 Analysis results with CMS software [48]

Generated events for unparticle signal and background, as discussed in Sections 4.3 and 4.4 respectively, are passed through Fast Simulation as described in Section 4.2.2. Photon ID, as discussed in Section 4.2.2, is used for identification of the photons with the following cuts applied on them:

- Photon $E_T > 50$ GeV;
- Photon $|\eta| < 1.5$.

Figure 4.11 shows the invariant mass distribution for scalar/tensor unparticle for several values of the unparticle model parameters and various backgrounds with usage of proper photon ID and the cuts above. These cuts were found to be optimal for the selection of photons for this analysis.

The invariant mass distribution is the same as the one shown in Section 4.3 (apart from the cuts applied in photons) with the difference that in Figure 4.11 there are an additional multiplication factors. One of them stands for the diphoton efficiency. The photon efficiency means, the efficiency of the reconstruction of photons in CMS detector. The photon efficiency was found to be $85 \pm 4\%$, therefore the overall diphoton efficiency is $72 \pm 7\%$. The other

multiplication factor stands for the K-factor which accounts for the NLO order effects. The cross sections of Table 4.1 are multiplied by a K-factor of 1.3 to account for these higher order effects.

Systematic errors, which account for uncertainties on different parameters like luminosity and photon reconstruction (see full list of systematic errors in Appendix B) that have been applied to both signal and background are:

1. Uncertainties on the luminosity and ID efficiency:

A 10% uncertainty to the combined product of the diphoton efficiency and integrated luminosity is assigned to the cross sections.

2. Uncertainty on the diphoton background:

- Uncertainty on normalization:

The main uncertainty on the diphoton background comes from the low statistics available for normalization at low masses, where unparticle effects are small. The relative background normalization uncertainty is taken to be $3.4/\sqrt{\int Ldt/pb}$, where $\int Ldt$ is the integrated luminosity. For $100pb^{-1}$ of data this uncertainty is 34%.

- Uncertainty on the K-factor:

A 10% uncertainty on the shape of the K-factor (the ratio of the NLO and LO cross sections) is used either for the diphoton background or the signal.

The overall relative uncertainty on the background is given by

$$\delta B/B = 10\% \oplus 340\% / \sqrt{\int Ldt/pb}. \quad (4.24)$$

4.6 Exclusion limits on unparticle production

4.6.1 Large extra dimensions and unparticles

There is a large similarity between unparticle and LED models. LED gravity is based on the so-called ADD scenario [50] where gravity alone have access to the extra dimensions. The large size of the extra dimesions give rise to Kaluza-Klein (KK) mass modes which appear

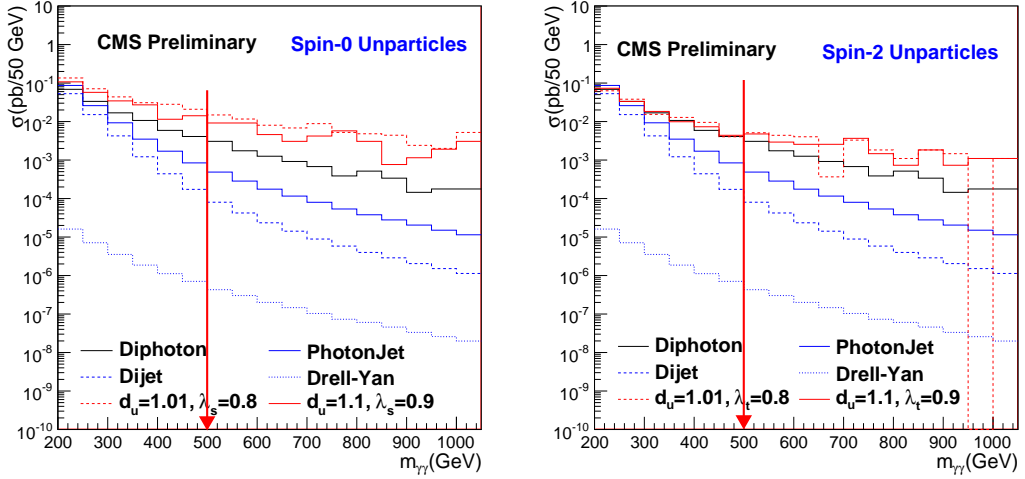


Figure 4.11: Diphoton invariant mass distribution for different backgrounds as well as scalar (left) and tensor (right) unparticle production. Lower limit on diphoton invariant mass of 500 GeV shown with a vertical red line, set to find limits on unparticle parameters and discovery potential.

as continuous graviton mass spectrum. Unparticles, on the other hand, give rise to phenomena very similar to the scenario of LED gravity with continuous mass spectrum as well. The matrix elements of the cross sections for the two processes, $U/G \rightarrow \gamma\gamma$, can be found in Section 4.3.1 and [51]. In general, these cross sections can be converted one to each other by simple translation of a few model related constants [52]

$$d_U = \frac{n}{2} + 1, \quad \Lambda_U = M_D \quad (4.25)$$

where n is the number of extra dimensions and M_D is the fundamental Planck scale of D dimensional gravity, where $D = n + 4$. M_D is related to the Planck scale, $M_{Pl} \sim 10^{19}$ GeV, according to the formula

$$M_D^{n+2} \sim \frac{M_{Pl}^2}{R^n} \quad (4.26)$$

where R is the size of extra dimension.

4.6.2 95 % CL limit on cross section

95 % CL limit on signal cross section is set by using standard Bayesian approach [53]. A flat prior is chosen for the signal cross section and a Poisson likelihood is constructed of observing n events in data given signal cross section S , signal acceptance A , background cross section B , and an integrated luminosity \mathcal{L}

$$P(n|S, A, B, \mathcal{L}) = e^{-(B+AS)\mathcal{L}} \frac{[(B + AS)\mathcal{L}]^n}{n!}. \quad (4.27)$$

Further systematic uncertainties are incorporated on B , A and \mathcal{L} by convoluting the above expression with Gaussian function centered at B , A and \mathcal{L} with the widths given by the uncertainties in the corresponding parameters [53]. This gives likelihood $L(n|S)$. The 95% upper limit on the signal cross section $\sigma^{95}(n)$ is found by solving the integral equation

$$\int_0^{\sigma^{95}(n)} L(n|S) dS = 0.95. \quad (4.28)$$

where n is the observed number of events in the counting window.

A priori it is not known how many events n can be found. This number may vary due to background fluctuations. Therefore we find the sum of individual limits $\sigma^{95}(n)$ and weighted it with the corresponding Poisson probabilities of observing n events given the background only hypothesis

$$\langle \sigma^{95} \rangle = \sum_{n=0}^{\infty} \sigma^{95}(n) \times e^{-BL} \frac{(BL)^n}{n!} \quad (4.29)$$

Following this procedure, the expected upper 95% CL limit on the signal cross section for unparticle decaying to two photons in the background only hypothesis is found for 50, 100 and 200 pb^{-1} luminosity and listed in Table 4.2.

4.6.3 Limits on unparticle parameters d_U and λ

To set limits on unparticle parameters, we find that the optimal cut on the invariant mass of the diphoton system is $M_{\gamma\gamma} > 500$ GeV. This is done by varying the cut and minimizing the

Table 4.2: 95% CL limit on the signal cross section ($\mathcal{U} \rightarrow \gamma\gamma$) for a signal in the diphoton channel for $500 \text{ GeV} < M_{\gamma\gamma} < 1000 \text{ GeV}$ and the expected number of background events in the same region [45].

Luminosity (pb^{-1})	$\sigma^{95}(pb)$	Number of background events
50	0.116	0.73 ± 0.12
100	0.068	1.46 ± 0.52
200	0.042	2.92 ± 0.75

expected 95% CL limit on the unparticle cross section. In addition, we set an upper limit on the diphoton invariant mass to be equal to $\Lambda_{\mathcal{U}} = 1000 \text{ GeV}$, as the theory is expected to be non-perturbative above this mass. Nevertheless, we also estimate the sensitivity of the search in case the upper bound on the mass is removed. This is done in Section 4.8.

The main irreducible background at these masses comes from direct diphoton production. We estimate this background by normalization to SM diphoton production in the $200 < M_{\gamma\gamma} < 500 \text{ GeV}$. However signal contamination in this region is not negligible, so we need to take this into account.

To find signal cross sections for the region $500 < M_{\gamma\gamma} < 1000 \text{ GeV}$ after the normalization procedure in the control region ($200 < M_{\gamma\gamma} < 500 \text{ GeV}$), we rescale them to account for the fact that any signal contamination in the control region will be considered as background by the normalization procedure, thus artificially increasing the SM background prediction in the signal region and consequently decreasing the unparticle effects. This is to say that if the ratio of the signal and SM background were the same in the signal and control regions, we would have no sensitivity to the signal at all because it would be normalized away.

The factor we use to decrease the cross section in the signal range $500 < M_{\gamma\gamma} < 1000 \text{ GeV}$ is given by the following equation

$$f = 1 - \frac{B_s}{\Delta S_s} \frac{\Delta S_c}{B_c}, \quad (4.30)$$

where B_c/B_s are SM cross sections in the $200 < M_{\gamma\gamma} < 500 \text{ GeV}$ control region and in the $500 < M_{\gamma\gamma} < 1000 \text{ GeV}$ signal region. $\Delta S_c/\Delta S_s$ are the differences between the total cross section (unparticle and SM cross section) and SM cross section, in the control and signal regions, respectively. Since tensor unparticle production interferes with the SM diphoton

production, ΔS can in principle be negative; in such cases we do not have sensitivity to unparticles. For scalar unparticles, ΔS is always positive, as there is no interference. For $\Delta S_c = 0$ the scale factor is exactly 1, while for $\Delta S_s/B_s = \Delta S_c/B_c$ the scale factor is exactly 0 thus resulting in no sensitivity to the signal.

Table 4.3 shows LO signal production cross sections at the generator level by using Pythia8 for the control (ΔS_c) and signal (ΔS_s) regions for spin-0 and spin-2 unparticles. Minimum cut on the invariant mass of two photons has been applied at the generation level, at 100 GeV for the control and 400 GeV for the signal region, respectively. 400 GeV cut was applied to have more statistics at high values of unparticle masses. The SM cross section in the control and signal regions B_c/B_s is 0.233/0.0152 pb. Scaling factors, f , given by Equation 4.30 are also shown in Table 4.3 for scalar and tensor cases. These factors are typically in the 0.85–0.95 range for the parameter sets we are most sensitive to and thus the effect of signal contamination in the normalization region is in fact small.

Table 4.3 also shows the scaled signal cross sections that are used to set limits on or obtain discovery sensitivity to the unparticle model parameters. The usual kinematic cuts on photons were applied as discussed in Section 4.5.

Table 4.3: LO scalar and tensor unparticle cross sections in the control $200 \text{ GeV} < M_{\gamma\gamma} < 500 \text{ GeV}$ (ΔS_c) and signal $500 \text{ GeV} < M_{\gamma\gamma} < 1000 \text{ GeV}$ (ΔS_s) regions, along with the correction factors f and rescaled cross section in the signal region ($\Delta S'_s$) used for limit setting and discovery potential estimate.

$d_{\mathcal{U}}$	λ	$\Delta S_c, \text{ pb}$		$\Delta S_s, \text{ pb}$		f		$\Delta S'_s, \text{ pb}$	
		Scalar unparticles		Tensor unparticles		Scalar	Tensor	Scalar	Tensor
1.01	0.9	4.46×10^{-1}	1.55×10^{-1}	5.02×10^{-2}	5.08×10^{-2}	0.81	0.94	1.25×10^{-1}	4.75×10^{-2}
1.1	0.9	1.44×10^{-1}	6.55×10^{-2}	4.24×10^{-3}	1.68×10^{-2}	0.86	0.98	5.61×10^{-2}	1.66×10^{-2}
1.2	0.9	4.54×10^{-2}	2.62×10^{-2}	-4.87×10^{-4}	5.49×10^{-3}	0.89	1.01	2.32×10^{-2}	5.53×10^{-3}
1.3	0.9	1.68×10^{-2}	1.09×10^{-2}	9.37×10^{-4}	1.43×10^{-3}	0.90	0.96	9.82×10^{-3}	1.37×10^{-3}
1.5	0.9	7.44×10^{-4}	1.87×10^{-3}	2.03×10^{-3}	6.73×10^{-4}	0.97	0.80	1.82×10^{-3}	5.41×10^{-4}
1.7	0.9	6.01×10^{-4}	3.81×10^{-4}	1.77×10^{-3}	6.32×10^{-4}	0.90	0.82	3.42×10^{-4}	5.16×10^{-4}
1.9	0.9	8.08×10^{-5}	2.46×10^{-4}	1.87×10^{-3}	1.00×10^{-3}	0.98	0.88	2.41×10^{-4}	8.83×10^{-4}
1.01	0.2	1.31×10^{-3}	1.54×10^{-4}	-1.96×10^{-5}	-1.24×10^{-3}	0.44	1.00	6.87×10^{-5}	-1.24×10^{-3}
1.01	0.4	2.35×10^{-2}	6.02×10^{-3}	-8.15×10^{-3}	-1.82×10^{-3}	0.74	0.71	4.48×10^{-3}	-1.29×10^{-3}
1.01	0.6	9.05×10^{-2}	2.89×10^{-2}	-9.51×10^{-3}	3.55×10^{-3}	0.80	1.17	2.30×10^{-2}	4.17×10^{-3}
1.01	0.8	2.99×10^{-1}	9.44×10^{-2}	1.63×10^{-2}	2.71×10^{-2}	0.79	0.96	7.49×10^{-2}	2.61×10^{-2}
1.01	1	7.00×10^{-1}	2.32×10^{-1}	9.08×10^{-2}	8.16×10^{-2}	0.80	0.93	1.86×10^{-1}	7.57×10^{-2}

The exclusion limits for the unparticle production are estimated for a data sample of 50–200 pb^{-1} as discussed in Section 4.6.2. The third column of the Table 4.2 quotes the number of background events for different luminosities with their uncertainties (overall systematic uncertain-

ties and diphoton background normalization uncertainty). The cross section limits, σ^{95} , from Table 4.2 are directly comparable with the parton-level unparticle cross section within the kinematic cuts ($E_T(\gamma) > 50$ GeV, $|\eta(\gamma)| < 1.5$, $500 < M_{\gamma\gamma} < 1000$ GeV) given in the last column of Table 4.3.

In addition, to account for NLO corrections, a K -factor of 1.3 [54] has been applied to the LO rescaled signal cross sections from Table 4.3.

These upper 95% CL cross section limits, σ^{95} , are translated into limits on unparticle model parameters by taking their intersections with the unparticle cross section curves. The unparticle cross section curve is obtained by fitting with a polynomial function the points $(\Delta S', d_U)$ and $(\Delta S', \lambda)$ from Table 4.3. Figures 4.12 and 4.13 show the limits on d_U and λ for spin-0 and spin-2 unparticles, respectively. In the absence of an apparent signal, with 200 pb^{-1} of data, we can set a lower 95% CL limit on d_U for scalar (tensor) unparticles at 1.16 (1.04) for $\lambda = 0.9$. For $d_U = 1.01$ we can exclude values of $\lambda > 0.65$ (0.8) at the 95% CL.

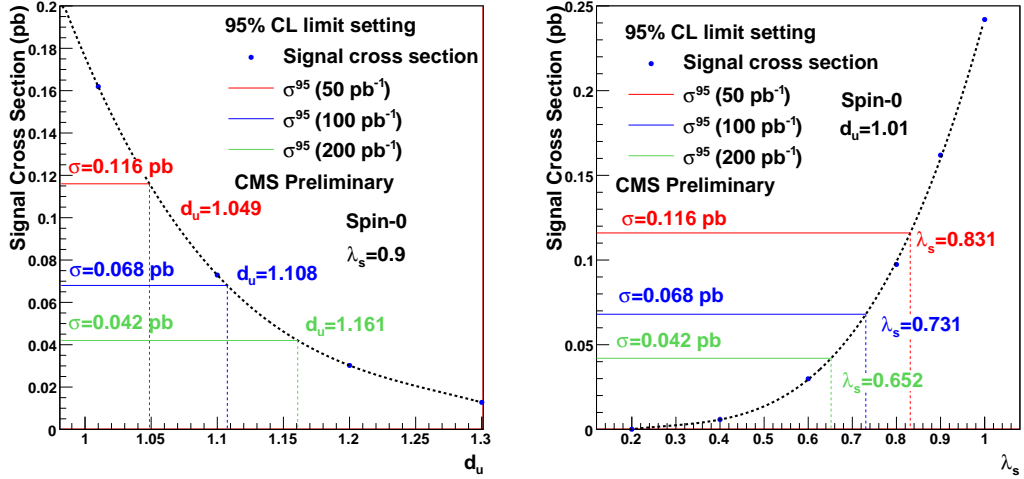


Figure 4.12: Spin-0 unparticle cross section parametrization as a function of d_U for $\lambda_s = 0.9$ (left) and λ_s for $d_U = 1.01$ (right) for $500 < M_{\gamma\gamma} < 1000$ GeV.

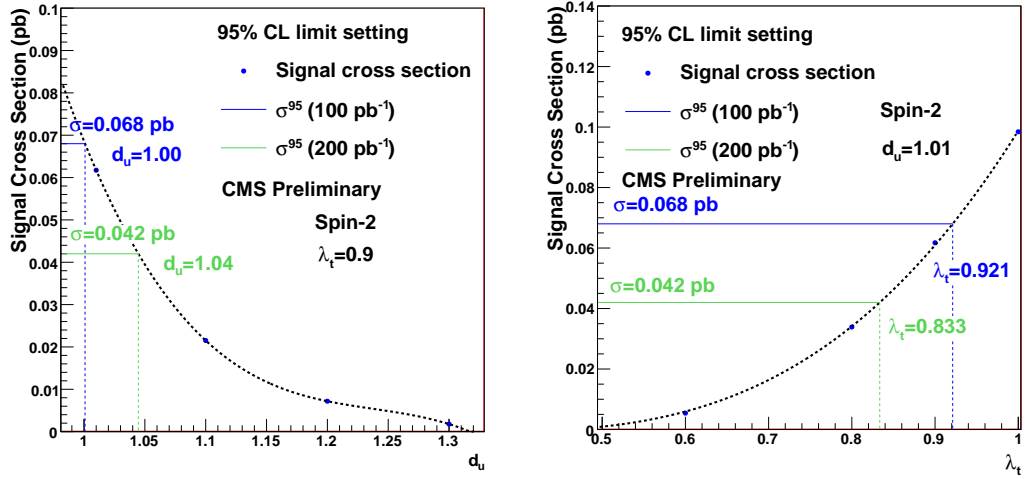


Figure 4.13: Spin-2 unparticle cross section parametrization as a function of d_U for $\lambda_t = 0.9$ (left) and λ_t for $d_U = 1.01$ (right) for $500 < M_{\gamma\gamma} < 1000$ GeV.

4.7 Discovery potential for unparticle

4.7.1 Discovery potential for $500 < M_{\gamma\gamma} < 1000$ GeV invariant mass cut

To find the discovery potential for unparticles, we calculate the Poisson probability for the background (B) to fluctuate to or above the number of events n observed in the counting window. When there is no systematic error on the background prediction, this probability is given by

$$p(\mathcal{L}) = \sum_{i=n}^{\infty} e^{-\mathcal{L}B} \frac{(\mathcal{L}B)^i}{i!} = 1 - \sum_{i=0}^{n-1} e^{-\mathcal{L}B} \frac{(\mathcal{L}B)^i}{i!} \quad (4.31)$$

where $b = \mathcal{L}B$ gives the expected number of background events in the counting window. In the case of systematic uncertainties, which is our case, we convolute the uncertainty on b by integrating over the Gaussian function

$$p = 1 - \sum_{i=0}^{n-1} \int_0^{\infty} dx \frac{1}{\sqrt{2\pi}\delta b} \exp\left(-\frac{(x-b)^2}{2(\delta b)^2}\right) e^{-x} \frac{x^i}{i!} \quad (4.32)$$

where δb is the uncertainty on the background prediction in terms of the number of background events.

Further the p value given by Equation 4.32 is converted to Gaussian significance of a one-sided fluctuation, represented as number of standard deviations, σ . In particular, 3σ evidence for signal correspond to the p -value of 1.35×10^{-3} and 5σ discovery corresponds to the p -value of 2.85×10^{-7} . We also want to ensure that the discovery is not claimed based on just one observed event which is possible from Equation 4.32 if there is small background. Therefore additionally it is required that the minimum number of expected events, $S + B$, signal + background, to be at least 3 for a 3σ -evidence or 5 for a 5σ -discovery.

To find the discovery potential for scalar and tensor unparticles, we perform one more procedure. Since the control region has sizable signal contamination, in the presence of true signal, the background in the signal region will be overestimated due to the control region normalization procedure. Given the true background B_s in the signal region, the following background will be inferred

$$B'_s = B_s \times \frac{B_c + \Delta S_c}{B_c}.$$

Hence, the true SM background in the signal region should be scaled by the following factor

$$f_B = 1 + \frac{\Delta S_c}{B_c}. \quad (4.33)$$

This factor depends on the unparticle model parameters and is listed in Table 4.4 for the model parameters used in this analysis.

Table 4.4: f_B factor for scalar and tensor unparticles.

d_U	λ	f_B (Scalar)	f_B (Tensor)
1.01	0.9	2.97	1.22
1.1	0.9	1.61	1.02
1.2	0.9	1.19	1.00
1.3	0.9	1.07	1.00
1.5	0.9	1.00	1.01
1.7	0.9	1.00	1.01
1.9	0.9	1.00	1.01
1.01	0.2	1.00	1.00
1.01	0.4	1.10	0.97
1.01	0.6	1.39	0.96
1.01	0.8	2.28	1.07
1.01	1	4.00	1.39

Hence, for each model, we scale the true diphoton background cross section of 0.0146 (for 100 pb⁻¹ luminosity) by f_B and also change the uncertainty due to the normalization in the

control region from the nominal one ($\delta B/B = 10\% \oplus 340\% / \sqrt{\int Ldt/\text{pb}}$, where $\int Ldt$ is the integrated luminosity) to the one that reflects higher background in the control region and hence smaller normalization uncertainty

$$\delta B/B = 10\% \oplus 340\% / \sqrt{f_B \int Ldt/\text{pb}}. \quad (4.34)$$

The net effect is that the background in the signal region becomes higher, but the uncertainty on it decreases. The effect of the increased background in the signal region is small for tensor unparticles, but sizable for the scalar ones.

The discovery potential for spin-0 and spin-2 unparticle, calculated using Equation 4.32, are shown in Figure 4.14 and listed in Table 4.5 for $500 \text{ GeV} < M_{\gamma\gamma} < 1000 \text{ GeV}$.

Table 4.5: Luminosity needed for observation or discovery given spin-0 and spin-2 unparticle parameters for $500 \text{ GeV} < M_{\gamma\gamma} < 1000 \text{ GeV}$.

Unparticle parameters	$\int Ldt$ needed for 3σ evidence	$\int Ldt$ needed for 5σ discovery
Scalar Unparticles		
$d_U = 1.01, \lambda_s = 1.0$	$\sim 40 \text{ pb}^{-1}$	$\sim 120 \text{ pb}^{-1}$
$d_U = 1.01, \lambda_s = 0.9$	$\sim 70 \text{ pb}^{-1}$	$\sim 180 \text{ pb}^{-1}$
$d_U = 1.01, \lambda_s = 0.8$	$\sim 135 \text{ pb}^{-1}$	$\sim 370 \text{ pb}^{-1}$
$d_U = 1.1, \lambda_s = 0.9$	$\sim 170 \text{ pb}^{-1}$	$\sim 485 \text{ pb}^{-1}$
$d_U = 1.2, \lambda_s = 0.9$	$\sim 640 \text{ pb}^{-1}$	$\sim 2040 \text{ pb}^{-1}$
Tensor Unparticles		
$d_U = 1.01, \lambda_t = 1.0$	$\sim 100 \text{ pb}^{-1}$	$\sim 250 \text{ pb}^{-1}$
$d_U = 1.01, \lambda_t = 0.9$	$\sim 180 \text{ pb}^{-1}$	$\sim 520 \text{ pb}^{-1}$
$d_U = 1.01, \lambda_t = 0.8$	$\sim 480 \text{ pb}^{-1}$	$\sim 1380 \text{ pb}^{-1}$

4.7.2 Discovery potential for $600(700) < M_{\gamma\gamma} < 1000 \text{ GeV}$ invariant mass cut

To demonstrate that the $M_{\gamma\gamma} > 500 \text{ GeV}$ cut is indeed the optimum one, we repeat the discovery significance calculations for the two higher values of the invariant mass cut 600 and 700 GeV. Figures 4.15 and 4.16 show the discovery potential for $600 \text{ GeV} < M_{\gamma\gamma} < 1000 \text{ GeV}$ and $700 \text{ GeV} < M_{\gamma\gamma} < 1000 \text{ GeV}$. It can be concluded that, increasing the lower invariant mass cut does not improve significantly the sensitivity to unparticles in the range of integrated luminosities characteristic for early data taking.

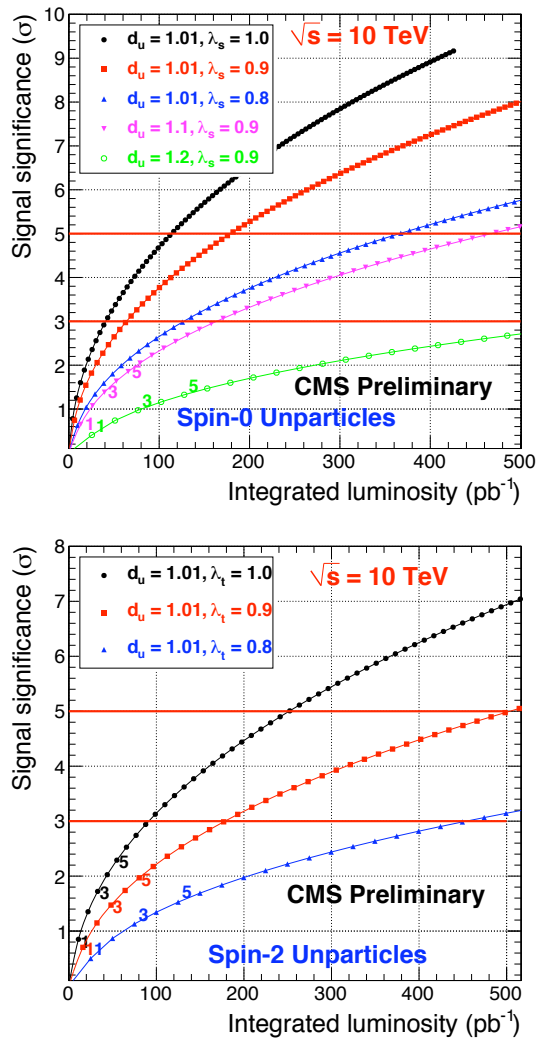


Figure 4.14: Luminosity required for for spin-0 and spin-2 unparticle discovery for $500 \text{ GeV} < M_{\gamma\gamma} < 1000 \text{ GeV}$. Different lines correspond to different model parameters. Subsequent points on the lines correspond to sequential integer number of expected events; points corresponding to 1, 3, and 5 events are marked correspondingly.

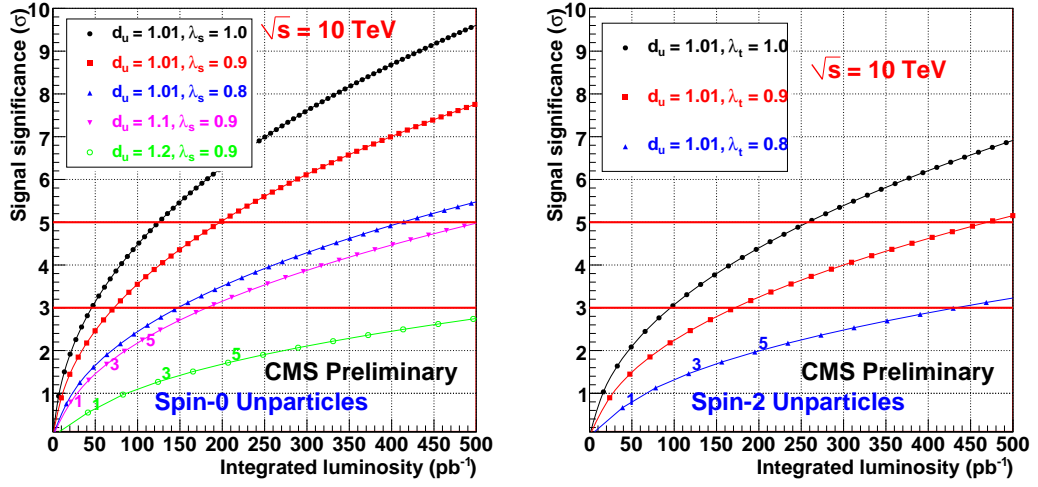


Figure 4.15: Luminosity required for for spin-0 and spin-2 unparticle discovery for $600 \text{ GeV} < M_{\gamma\gamma} < 1000 \text{ GeV}$. Different lines correspond to different model parameters. Subsequent points on the lines correspond to sequential integer number of expected events; points corresponding to 1, 3, and 5 events are marked correspondingly.

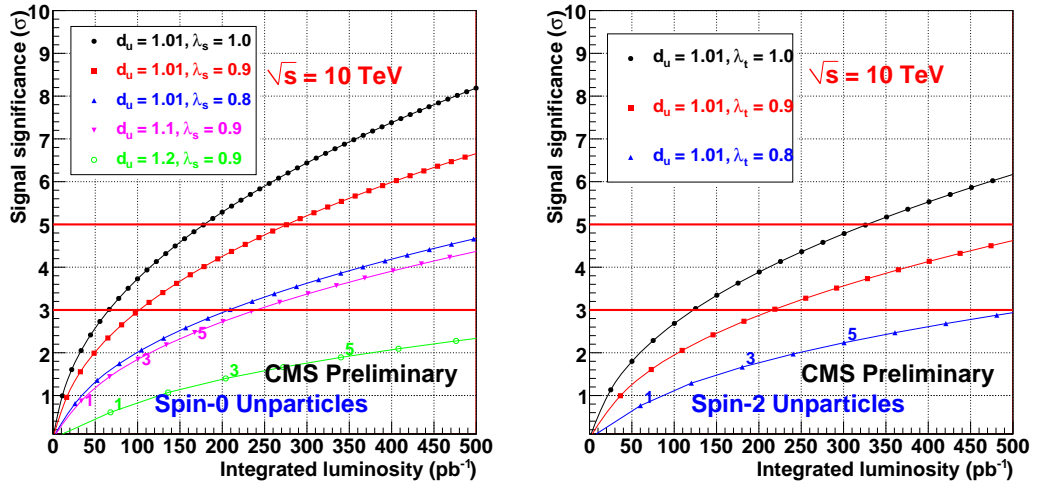


Figure 4.16: Luminosity required for for spin-0 and spin-2 unparticle discovery for $700 \text{ GeV} < M_{\gamma\gamma} < 1000 \text{ GeV}$. Different lines correspond to different model parameters. Subsequent points on the lines correspond to sequential integer number of expected events; points corresponding to 1, 3, and 5 events are marked correspondingly.

4.8 Sensitivity to the unparticle model parameters without the perturbativity bound

The perturbativity bound $M_{\gamma\gamma} < \Lambda_{\mathcal{U}}$ is not exact. It is not clear that the unparticle production suddenly turns off around $\sqrt{s} = \Lambda_{\mathcal{U}}$ or that the production rates are modified significantly. Therefore we perform similar study as discussed in Section 4.6.3 but remove the perturbativity bound to see how that affects our sensitivity.

We repeat exactly the same approach, this time without setting an upper limit on the signal cross section $M_{\gamma\gamma} < \Lambda_{\mathcal{U}} = 1$ TeV. Table 4.6, in analogy with Table 4.3, shows the scaled signal cross sections in the $M_{\gamma\gamma} > 500$ GeV region for spin-0 and spin-2 unparticle. For the normalization procedure, again is used the $200 < M_{\gamma\gamma} < 500$ GeV control region. Figures 4.17 and 4.18 show the new limits on unparticle parameters for $M_{\gamma\gamma} > 500$ GeV. Compared to the results with the upper invariant mass cut, the new limits are considerably more stringent, particularly in the case of scalar unparticles.

Table 4.6: LO scalar and tensor unparticle cross sections in the control $200 \text{ GeV} < M_{\gamma\gamma} < 500$ GeV (ΔS_c) and signal $M_{\gamma\gamma} > 500$ GeV (ΔS_s) regions, along with the correction factors f and rescaled cross section in the signal region ($\Delta S'_s$) used for limit setting and discovery potential estimate.

$d_{\mathcal{U}}$	λ	ΔS_c , pb		ΔS_s , pb		f		$\Delta S'_s$, pb	
		Scalar unparticles	Tensor unparticles	Scalar unparticles	Tensor unparticles	Scalar	Tensor	Scalar	Tensor
1.01	0.9	4.46×10^{-1}	2.02×10^{-1}	5.02×10^{-2}	8.57×10^{-2}	0.84	0.96	1.70×10^{-1}	8.21×10^{-2}
1.1	0.9	1.44×10^{-1}	9.20×10^{-2}	4.24×10^{-3}	3.58×10^{-2}	0.89	1.00	8.20×10^{-2}	3.55×10^{-2}
1.2	0.9	4.54×10^{-2}	4.08×10^{-2}	-4.87×10^{-4}	1.57×10^{-3}	0.92	1.00	3.76×10^{-2}	1.58×10^{-2}
1.3	0.9	1.68×10^{-2}	1.86×10^{-2}	9.37×10^{-4}	7.58×10^{-3}	0.94	0.99	1.75×10^{-2}	7.52×10^{-3}
1.5	0.9	7.44×10^{-4}	4.76×10^{-3}	2.03×10^{-3}	3.84×10^{-3}	0.99	0.96	4.71×10^{-3}	3.70×10^{-3}
1.7	0.9	6.01×10^{-4}	1.97×10^{-3}	1.77×10^{-3}	3.36×10^{-3}	0.98	0.96	1.93×10^{-3}	3.24×10^{-3}
1.9	0.9	8.08×10^{-5}	3.28×10^{-3}	1.87×10^{-3}	6.35×10^{-3}	1.00	0.98	3.28×10^{-3}	6.22×10^{-3}
1.01	0.2	1.31×10^{-3}	2.31×10^{-4}	-1.96×10^{-5}	-1.47×10^{-3}	0.60	1.00	1.40×10^{-4}	-1.47×10^{-3}
1.01	0.4	2.35×10^{-2}	8.14×10^{-3}	-8.15×10^{-3}	-1.44×10^{-3}	0.80	0.61	6.50×10^{-3}	-8.72×10^{-4}
1.01	0.6	9.05×10^{-2}	3.81×10^{-2}	-9.51×10^{-3}	8.79×10^{-3}	0.84	1.08	3.18×10^{-2}	9.45×10^{-3}
1.01	0.8	2.99×10^{-1}	1.25×10^{-1}	1.63×10^{-2}	4.75×10^{-2}	0.83	0.98	1.04×10^{-1}	4.64×10^{-2}
1.01	1	7.00×10^{-1}	3.03×10^{-1}	9.08×10^{-2}	1.36×10^{-1}	0.84	0.95	2.54×10^{-1}	1.29×10^{-1}

Figure 4.19 and Table 4.7 show the discovery sensitivity to spin-0 and spin-2 unparticles for $M_{\gamma\gamma} > 500$ GeV. The same procedure of rescaling the SM background in signal region by factor f_B (see Table 4.4) is used. Removing the perturbativity bound roughly reduces by half the luminosity needed for discovery of unparticles.

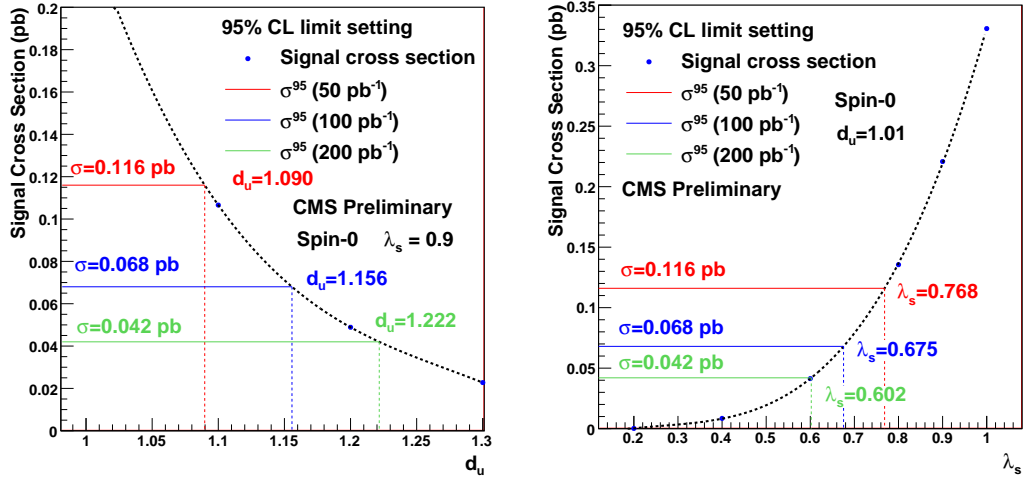


Figure 4.17: Spin-0 unparticle cross section parametrization as a function of d_u for $\lambda_s = 0.9$ (left) and λ_s for $d_u = 1.01$ (right) for $M_{\gamma\gamma} > 500$ GeV.

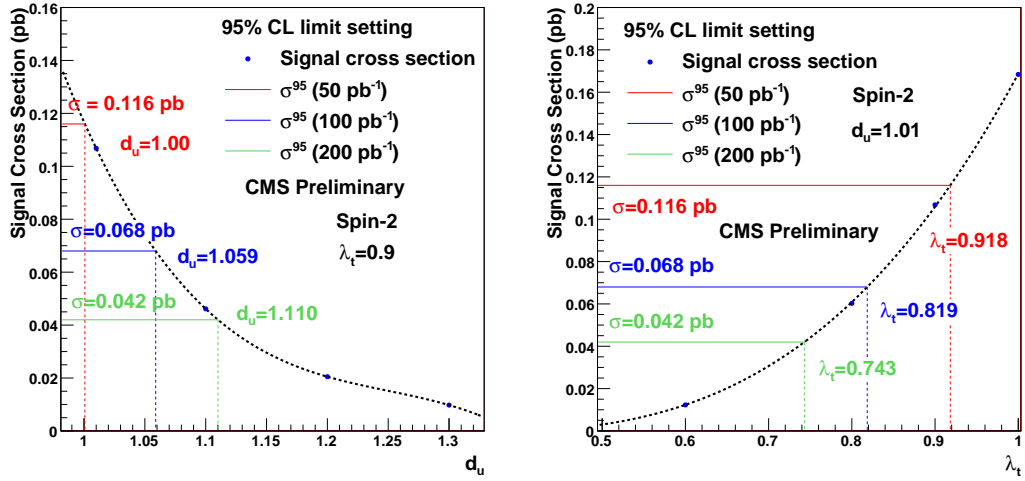


Figure 4.18: Spin-2 unparticle cross section parametrization as a function of d_u for $\lambda_t = 0.9$ (left) and λ_t for $d_u = 1.01$ (right) for $M_{\gamma\gamma} > 500$ GeV.

Table 4.7: Luminosity needed for observation or discovery given spin-0 and spin-2 unparticle parameters for $M_{\gamma\gamma} > 500$ GeV.

Unparticle parameters	$\int Ldt$ needed for 3σ evidence	$\int Ldt$ needed for 5σ discovery
Scalar Unparticles		
$d_U = 1.01, \lambda_s = 1.0$	$\sim 30 pb^{-1}$	$\sim 70 pb^{-1}$
$d_U = 1.01, \lambda_s = 0.9$	$\sim 40 pb^{-1}$	$\sim 110 pb^{-1}$
$d_U = 1.01, \lambda_s = 0.8$	$\sim 75 pb^{-1}$	$\sim 200 pb^{-1}$
$d_U = 1.1, \lambda_s = 0.9$	$\sim 90 pb^{-1}$	$\sim 250 pb^{-1}$
$d_U = 1.2, \lambda_s = 0.9$	$\sim 265 pb^{-1}$	$\sim 760 pb^{-1}$
Tensor Unparticles		
$d_U = 1.01, \lambda_t = 1.0$	$\sim 40 pb^{-1}$	$\sim 110 pb^{-1}$
$d_U = 1.01, \lambda_t = 0.9$	$\sim 75 pb^{-1}$	$\sim 210 pb^{-1}$
$d_U = 1.01, \lambda_t = 0.8$	$\sim 170 pb^{-1}$	$\sim 490 pb^{-1}$

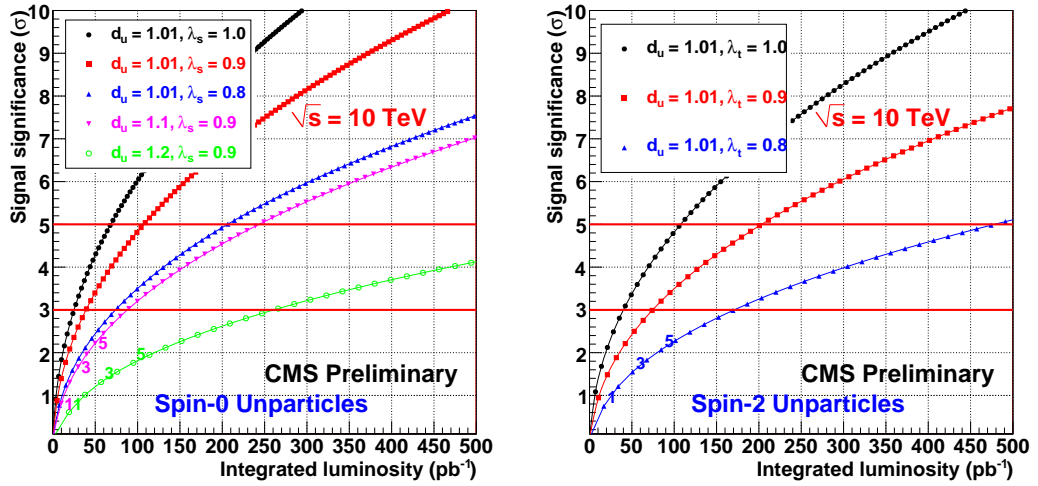


Figure 4.19: Luminosity required for for spin-0 and spin-2 unparticle discovery for $M_{\gamma\gamma} > 500$ GeV. Different lines correspond to different model parameters. Subsequent points on the lines correspond to sequential integer number of expected events; points corresponding to 1, 3, and 5 events are marked correspondingly.

CHAPTER 5

CONCLUSIONS

In this thesis, the sensitivity to unparticle production into the diphoton decay channel is studied with the CMS detector at LHC.

The 95% CL limit on the cross section of unparticle decaying into a pair of photons is found by using standart Bayesian approach for data samples of 50, 100 and 200 pb^{-1} luminosity. These upper 95% cross section limits are subsequently translated into limits on unparticle model parameters, scaling dimension $d_{\mathcal{U}}$ and coupling constant λ .

Two approaches are used to determine the unparticle cross sections to be compared with the 95% CL limit. In both studies, a lower cut on the invariant mass of the diphoton system is found to be 500 GeV by optimization procedure. In the first approach, we set an upper limit on the diphoton invariant mass of 1000 GeV since the theory is not perturbative above this mass. In the second approach, no upper bound on the diphoton invariant mass is set in order to see how this affects our results. We find that with the upper invariant mass cut, the limits on unparticle parameters are more stringent. Additionally, in order to account for signal contamination in the region $M_{\gamma\gamma} < 500$ GeV, where the signal can be mixed with the SM background, the unparticle cross sections for $M_{\gamma\gamma} > 500$ GeV, with and without upper invariant mass cut, are modified using normalization procedure. It is shown as well, that the lower bound on the invariant mass $M_{\gamma\gamma} > 500$ indeed is the optimal one for setting limits and discovery potential for unparticles decaying to two photons.

Limits on unparticle parameters $d_{\mathcal{U}}$ and λ for three different sets of data sample luminosities 50, 100 and 200 pb^{-1} are found. The limits on $d_{\mathcal{U}}$ and λ_s for scalar unparticle with 100 pb^{-1} for invariant mass $500 < M_{\gamma\gamma} < 1000$ GeV and $\Lambda_{\mathcal{U}} = 1$ TeV are as follows:

- For $d_U = 1.01$, $\lambda_s > 0.7$ can be excluded;
- For $\lambda_s = 0.9$, $d_U < 1.1$ can be excluded.

We also conclude that the sensitivity to tensor unparticles is not that high in comparison with the scalar unparticles in the suggested parameter space (d_U, λ) .

The discovery potential for spin-0 and spin-2 unparticle is found by calculating the Poisson probability for the background to fluctuate to or above the number of events in a counting window. Then the probability is converted into a Gaussian significance, σ . For invariant mass $500 < M_{\gamma\gamma} < 1000$ GeV and $\Lambda_U = 1$ with ~ 200 pb⁻¹ the scalar unparticle can be observed at 5σ for $d_U = 1.01$ and $\lambda > 0.9$.

This is the first simulation study of the sensitivity to unparticles decaying into the diphoton final state at a hadron collider.

REFERENCES

- [1] S. Weinberg, Phys. Rev. Lett. **19** (1967) 1264.
- [2] A. Salam, Originally printed in Svartholm: Elementary Particle Theory, Proceedings Of The Nobel Symposium Held 1968 At Lerum, Sweden, Stockholm 1968, 367-377
- [3] S.L. Glashow et. al, Phys. Rev. D **2** (1970) 1285.
- [4] H. Georgi, Annu. Rev. Nucl. Part. Sci. **43:209-52** (1993).
- [5] E. Goldfain, Progress in Physics **v.3** (2008).
- [6] B. Bhattacharya, Final Project: Special Topics in Elementary Particle Physics.
- [7] H. Georgi, Phys. Rev. Lett. **98** (2007) 221601.
- [8] T. Banks and A. Zaks, Nucl. Phys. **196** (1982) 189.
- [9] H. Georgi, The Unparticle Scale, Power point presentation.
- [10] K. Cheung et. al, Phys. Rev. D **76** (2007) 055003.
- [11] A. Rajaraman, arXiv:0809.5092v2[hep-ph].
- [12] K. Cheung et al., Phys. Rev. Lett. **99** (2007) 051803.
- [13] S.L. Chen et. al, JHEP 0711 **010** (2007).
- [14] S.L. Chen et. al, Phys. Rev. D **77** (2008) 097701.
- [15] K. Cheung et. al, Phys. Lett. B **662** (2008) 436.
- [16] T.G. Rizzo, Phys. Lett. B **665** (2008) 361.
- [17] H. Georgi, Phys. Lett. B **650** (2007) 275.
- [18] J.L. Feng et al., Phys. Rev. D **77** (2008) 075007.
- [19] H. Georgi and Y. Kats, arXiv:0904.1962v1[hep-ph].
- [20] A. Rajaraman, Phys. Lett. B **671** (2009) 411.
- [21] P. Mathews and V. Ravindran, Phys. Lett. B **657** (2007) 198.
- [22] P.J. Fox, Phys. Rev. D **76** (2007) 075004.
- [23] V. Barger et al., arXiv:0801.3771v1[hep-ph].
- [24] T. Rizzo, JHEP0710 **044** (2007).

- [25] A. Delgado, JHEP10 **094** (2007).
- [26] G. Cacciapaglia et al., JHEP 0801 **070** (2008).
- [27] J. McDonald, arXiv:0805.1888v2[hep-ph].
- [28] A. Freitas and D. Wyler, JHEP12 **033** (2007).
- [29] S. Hannestad et al., Phys. Rev. D **76** (2007) 121701.
- [30] T. Kikuchi and N. Okada, Phys. Lett. B **665** (2008) 186.
- [31] O.S. Bruning et. al, LHC Design Report, CERN-2004-03, (2004) CERN.
- [32] The CMS Collaboration, S. Chatrchyan et al., JINST **3** (2008) S08004.
- [33] T. Han, arXiv:0508098v1[hep-ph].
- [34] R.M. Godbole, arXiv:9602428v1[hep-ph].
- [35] R. Nisius, Phys. Rept. **332** (2000) 165-317.
- [36] T. Sjostrand, S. Mrenna and P. Skands, Pythia 6.4 Physics and Manual.
- [37] S. Agostinelli et al., Nucl. Inst. and Meth. A **506** (2003) 250.
- [38] D. Stump et al., JHEP **10** (2003) 046.
- [39] G. Watt et al., arXiv:0806.4890v1[hep-ph].
- [40] B. Andersson et al., Phys. Rep. **97** (1983) 31.
- [41] A. Askew, et al., A Review of Reconstruction in the Electromagnetic Calorimeter, In preparation.
- [42] M.C. Kumar et al., Phys. Rev. D **77** (2008) 055013.
- [43] B. Grinstein et al., Phys. Lett. B **662** (2008) 367.
- [44] A.D. Martin et al., Phys. Lett. B **531** (2002) 216.
- [45] CMS Collaboration, CMS Note **EXO-09-004**.
- [46] B. Bailey and J.F. Owens, Phys. Rev. D **46** (1992) 2018-2027.
- [47] E.L. Berger, et al., Nucl. Phys. B **239** (1984) 52.
- [48] CMS Collaboration, CMS Note **EXO-09-011**.
- [49] CMS Collaboration, CMS Physics Technical Design Report, Vol.II Physics Performance.
- [50] N. Arkani-Hamed et al., Phys. Lett. B **436** (1998) 257.
- [51] G.F. Giudice et al., Nucl. Phys. B **544** (1999) 3.
- [52] S. Ask et al., Real emission and Virtual Exchange of Gravitons and Unparticles with Pythia8, In preparation.
- [53] I. Bertram et al., Fermilab-TM-2104 (2000).
- [54] M.C. Kumar et al., Phys. Rev. D **79** (2009) 075012.

APPENDIX A

KINEMATICAL VARIABLES IN HADRON COLLISIONS [33]

In LHC where we have proton proton collision, the actual collision, in fact, can be thought to occur between the partons with fractional momentum of $p_1 = x_1 P_A$ and $p_2 = x_2 P_B$. P_A and P_B are the momenta of incoming protons and can be denoted in the following way

$$P_A = (E_A, 0, 0, p_A), \quad P_B = (E_B, 0, 0, -p_A). \quad (\text{A.1})$$

The parton CM frame is moving with momentum P_{CM} given by

$$P_{CM} = ((x_1 + x_2)E_A, 0, 0, (x_1 - x_2)p_A) \quad \text{where} \quad (E_A \approx p_A) \quad (\text{A.2})$$

and the rapidity y_{CM} of the parton CM frame is

$$y_{CM} = \frac{1}{2} \ln \frac{x_1}{x_2} \quad (\text{A.3})$$

with parton energy fractions x_1 and x_2 given by

$$x_{1,2} = \sqrt{\tau} e^{\pm y_{CM}}. \quad (\text{A.4})$$

τ is defined as

$$\tau = x_1 x_2 = \frac{s}{S} \quad (\text{A.5})$$

with $s \equiv \tau S$, where $S = 4E_A^2$ is the total hadronic CM energy and s is the partonic CM energy.

Lets consider a final state particle with momentum $p^\mu = (E, \vec{p})$ in the lab frame. Since the CM frame of the two colliding partons is a priori undetermined with respect to the lab frame, it is better to seek for kinematical variables that are invariant under longitudinal boosts.

- Transverse momentum p_T and azimuthal angle θ : This is the momentum in the direction perpendicular to the beam pipe and is invariant under longitudinal boost.

$$p_T = \sqrt{p_x^2 + p_y^2} = p \sin \theta \quad (\text{A.6})$$

In longitudinal direction, momentum can not be determined.

- Rapidity and pseudo-rapidity:

$$y = \frac{1}{2} \ln \frac{E + P_z}{E - p_z} = \frac{1}{2} \ln \frac{1 + \beta_z}{1 - \beta_z} \quad (\text{A.7})$$

where $\beta_z = p_z/E = \beta \cos \theta$ is the z -component of the particle's velocity. In the massless limit, $E \approx |\vec{p}|$

$$y \rightarrow \frac{1}{2} \ln \frac{1 + \cos \theta}{1 - \cos \theta} = \ln \cot \frac{\theta}{2} \equiv \eta \quad (\text{A.8})$$

where η is pseudo-rapidity and $-\infty < \eta < \infty$.

- Separation in (θ, ϕ) plane ΔR : Introduction of separation, provides practical definition of a hadronic jet. ΔR specifies the cone size of a jet formed by multiple hadrons within ΔR .

$$\Delta R = \sqrt{\Delta\eta^2 + \Delta\phi^2} \quad (\text{A.9})$$

- Invariant mass: If we search for a resonant signal in the s -channel, the invariant mass variable turns out to be very useful. If unstable particle V is produced by particles a and b and decay to $1 + 2 + \dots + n$ particles, then its invariant mass, M_V , can be reconstructed either by using the initial momenta or the final momenta of these particles.

$$(p_a + p_b)^2 = \left(\sum_i^n p_i \right)^2 \approx M_V^2 \quad (\text{A.10})$$

- Missing transverse momentum P_T^{miss} and energy E_T^{miss} : If a particle can not be observed by the detector, only its transverse momentum and energy can be inferred by balancing the observed momenta/energy.

$$P_T^{miss} = - \sum_i P_{T_i}, \quad E_T^{miss} = - \sum_i E_{T_i} \quad (\text{A.11})$$

p_{T_i} and E_{T_i} denote the observed transverse momenta and energy which balance the missing transverse momentum P_T^{miss} and energy E_T^{miss} .

APPENDIX B

SYSTEMATIC UNCERTAINTIES [49]

A systematic error is an error that will occur consistently in only one direction each time the experiment is performed, i.e., the value of the measurement will always be greater (or lesser) than the real value. There are two type of systematic errors due to 1) theoretical uncertainties and 2) experimental uncertainties. This is a list of the systematic uncertainties that are subject to study at LHC:

Theoretical uncertainties

- Hard process description:

To describe the hard process, one should use a Monte Carlo Generator. The simulation is done via matrix element calculations at a certain order in the coupling constants with the parton showering of the partons until a cut-off scale when the perturbative evolution stops and fragmentation of the final partons takes on. The calculation of the matrix elements depends on certain input parameters which are subject to their experimental uncertainties.

- Hard process scale:

The hard process under study uses a definite scale Q^2 , which enters in the parametrization of PDFs and α_s , which is to say the expression of the cross sections. The choice for Q^2 scale is unphysical and is regarded as important contribution to the uncertainty.

- PDF description:

The PDFs describe the probability density for partons undergoing hard scattering at the hard process scale Q^2 and taking a certain fraction x of the total particle momentum. Since PDFs depend on Q^2 which is not a definite value there is uncertainty in the definition of PDFs as well.

- **QCD radiation:**
Initial and final state radiation are produced following unitary evolutions with probabilities defined by the showering algorithm (Altarelli-Parisi equation) that depend on the Q^2 evolution variable.
- **Fragmentation:**
Fragmentation depends on the factorization scale. The formation of final state hadrons from primary quarks in a non-perturbative way is called fragmentation or hadronization. Parameters that regulate the fragmentation can change if the description of the underlying event change or if there is larger fraction of gluon jets.
- **Minimum bias and underlying event:**
Minimum bias events are dominated by soft-pT interactions with low transverse energy and low multiplicity although there are also some small contributions from hard scattering. Every interesting event is accompanied by the so-called underlying event, which is everything but the hard scattering and includes minimum bias. In general, the underlying event identifies all the remnant activity from the same proton-proton interaction. Correct modeling of the multiple partonic interactions can give an adequate description of the minimum bias and underlying event and the connection between them.
- **Pile-up:**
The Pile-up effect occur when on top of possible signal events, additional minimum bias interactions are produced in the same bunch crossing. The Pile-up can be affected by the definition of the minimum bias itself.

Each of these effects has to be modeled to the best of our knowledge and the uncertainties need to be determined and propagated to the physics measurement.

Experimental uncertainties

These uncertainties are associated with detector measurements.

- **Luminosity uncertainty:**
The design goal for the precision of the luminosity measurement at CMS is 5 %, which is assumed to be achieved after 1 fb^{-1} of data has been collected. For integrated luminosity less than 1 fb^{-1} , it is assumed that the precision is limited to 10 %.

- Track and vertex reconstruction uncertainty:

The uncertainty of the track reconstruction efficiency is taken to be 1 % for all tracks.

The primary vertex precision along the z coordinate is expected to be about $10 \mu\text{m}$ once 1 fb^{-1} has been collected. The transverse precision is expected to be about $1 \mu\text{m}$.

- ECAL calibration and energy scale uncertainties:

The precision to which the ECAL crystals can be intercalibrated is $0.4 - 2.0 \%$ using 5 fb^{-1} of data. The absolute energy scale can be determined using the Z mass constraint in $Z \rightarrow ee$ decay and is expected to be measured to a precision of about 0.05% .

- Jet and missing energy uncertainties:

An overall uncertainty of 15% is expected for jet response and energy scale uncertainty.

- Muon reconstruction uncertainties:

The precision of muon measurement is $200 \mu\text{m}$ in the plane transverse to the beam axis.